Mitotic checkpoint gene expression is tuned by coding sequences

Eric Esposito[1,2,†], Douglas E. Weidemann[1,2,†], Jessie M. Rogers[1,2], Claire M. Morton[1,2], Erod Keaton Baybay[1,2], Jing Chen[1], Silke Hauf[1,2,*]

[1]*Department of Biological Sciences, Virginia Tech, Blacksburg, VA 24061, USA*

[2]*Fralin Life Sciences Institute, Virginia Tech, Blacksburg, VA 24061, USA*

[†]These authors contributed equally to this work

*Correspondence: silke@vt.edu

Keywords: mitosis / spindle assembly checkpoint / mRNA decay / gene expression noise / cotranslational assembly

Abstract

The mitotic checkpoint (also called spindle assembly checkpoint, SAC) is a signaling pathway that safeguards proper chromosome segregation. Proper functioning of the SAC depends on adequate protein concentrations and appropriate stoichiometries between SAC proteins. Yet very little is known about SAC gene expression. Here, we show in fission yeast (*S. pombe*) that a combination of short mRNA half-lives and long protein half-lives supports stable SAC protein levels. For the SAC genes *mad2*$^{+}$ and *mad3*$^{+}$, their short mRNA half-lives are supported by a high frequency of non-optimal codons. In contrast, *mad1*$^{+}$ mRNA has a short half-life despite a low frequency of non-optimal codons and despite the lack of known destabilizing motifs. Hence, different SAC genes employ different strategies of expression. We further show that Mad1 homodimers form co-translationally, which may necessitate a certain codon usage pattern. Taken together, we propose that the codon usage of SAC genes is fine-tuned for proper SAC function. Our work shines light on gene expression features that promote spindle assembly checkpoint function and suggests that synonymous mutations may weaken the checkpoint.

Introduction

The spindle assembly checkpoint (SAC; also called mitotic checkpoint) is a eukaryotic signalling pathway that delays cell cycle progression when chromosomes have not yet become properly attached to microtubules during mitosis (Kops *et al*, 2020; Lara-Gonzalez *et al*, 2012; Musacchio, 2015). Proper function of the SAC needs appropriate SAC protein concentrations (both too low or too high expression can be detrimental) and needs adequate stoichiometries between proteins in the pathway (Chung & Chen, 2002; Gross *et al*, 2018; Heinrich *et al*, 2013; Ryan *et al*, 2012; Schuyler *et al*, 2012). This makes it important to quantitatively understand SAC gene expression. Yet, expression of these genes has not been studied in any detail.

The protein network of the SAC, on the other hand, is well understood. While the SAC is active, it forms the mitotic checkpoint complex (MCC), which prevents the anaphase-promoting complex (APC/C) from initiating anaphase (Pines, 2011). A key effector of the SAC is the Mad1/Mad2 complex, a tetramer of two Mad1 and two Mad2 molecules (Chen *et al*, 1999; Sironi *et al*, 2002) (Fig 1A). Mad1 homodimerizes through a long, parallel inter-molecular coiled-coil at its N-terminus, which is followed by the Mad2-binding motif and a C-terminal RWD (RING finger-, WD-repeat-, and DEAD-like proteins) domain (Chen *et al.*, 1999; Kim *et al*, 2012; Piano *et al*, 2021; Sironi *et al.*, 2002). The Mad1-binding partner Mad2 is a HORMA domain protein (named after Hop1, Rev7 and Mad2) that can change its conformation between open (O) and closed (C) (Aravind & Koonin, 1998; Luo *et al*, 2002; Luo *et al*, 2004). To bind Mad1, the C-terminus of Mad2 wraps around the Mad1 polypeptide similar to a seat belt and Mad2 adopts the closed conformation (Luo *et al.*, 2002; Sironi *et al.*, 2002). This results in a tight complex with no measurable dissociation rate *in vitro* (Chen *et al.*, 1999; Sironi *et al*, 2001; Vink *et al*, 2006). If and to what extent formation of the intricate Mad1/Mad2 complex is aided by other factors is unknown.

Through a different surface, Mad2 can form heterodimers between its two conformations (O-C) (Mapelli *et al*, 2007). Dimerization of Mad1/C-Mad2 with O-Mad2 facilitates binding of this O-Mad2 molecule to the APC/C activator Cdc20 (Slp1 in *S. pombe*). O-Mad2 changes its conformation in the process, forming C-Mad2/Cdc20 through the same seat belt type of binding (Luo *et al.*, 2002).

Subsequent binding of BubR1 (Mad3 in yeast) to C-Mad2/Cdc20 results in the mitotic checkpoint complex (MCC) (Chao *et al*, 2012; Sudakin *et al*, 2001). The MCC then inhibits the APC/C to block anaphase (Alfieri *et al*, 2016; Pines, 2011).

Because the SAC plays a central role in preventing chromosome mis-segregation and because persistent chromosome mis-segregation is a driver of tumor evolution, SAC malfunction is suspected to contribute to carcinogenesis (Funk *et al*, 2016; Gordon *et al*, 2012). Mouse models have shown that impairing the SAC promotes chromosome mis-segregation and tumor formation (Baker *et al*, 2005; Holland & Cleveland, 2009; Schvartzman *et al*, 2010). Completely abolishing the SAC, however, is detrimental to human cells (Dobles *et al*, 2000; Kops *et al*, 2004; Michel *et al*, 2004; Schukken *et al*, 2021), and suppression of the SAC may in fact be a successful therapeutic strategy against some cancer types (Cohen-Sharir *et al*, 2021; Quinton *et al*, 2021). Together, these results indicate that tuning SAC function can make the difference between normal growth, cancerous growth and cell death.

Although the SAC network has been studied in much detail from a protein-centric view, little is known about SAC gene expression. Understanding this regulatory layer is important, because changes in SAC protein concentrations can cause SAC malfunction—at least partly because proper stoichiometries, such as between Mad1 and Mad2, are important for function (Chung & Chen, 2002; Gross *et al.*, 2018; Heinrich *et al.*, 2013; Ryan *et al.*, 2012; Schuyler *et al.*, 2012). Here, using fission yeast (*Schizosaccharomyces pombe*), we study the mRNA layer of SAC gene expression and provide evidence that a combination of short mRNA and long protein half-lives ensures a stable concentration of SAC proteins over time and between cells. Our findings indicate that codon usage bias in *mad2⁺* and *mad3⁺*, but not *mad1⁺*, contributes to their short mRNA half-lives, and that the coding sequence of *mad1⁺* carries alternative features that influence expression of this gene. We provide evidence that Mad1 homodimers form co-translationally, which may necessitate a certain codon usage pattern. Overall, our findings shine light on gene expression features that promote SAC function and raise the possibility that synonymous mutations may impair the SAC.

Results

SAC mRNA numbers are approximately Poisson-distributed with means of two to four per cell

We previously quantified the concentration of SAC proteins fused to green fluorescent protein (GFP) in *S. pombe* and determined protein concentrations in a range between 30 and 150 nM with strikingly little inter-cell variability (i.e. low 'noise') (Heinrich *et al.*, 2013). In these strains, GFP had been fused by traditional tagging, changing the endogenous 3' UTR to that of the *Saccharomyces cerevisiae ADH1* gene and appending an antibiotic-resistance gene, which both may alter gene expression. To avoid such effects, we now employed CRISPR/Cas9-mediated scarless genome editing (Jacobs *et al*, 2014). We fused ymEGFP (yeast codon-optimized, monomeric enhanced GFP; in the following just 'GFP') to the SAC genes *mad1*$^{+}$, *mad2*$^{+}$ and *mad3*$^{+}$ without any change to the surrounding sequences (Fig 1B). Immunoblots showed concentrations broadly similar to the previous strains (Fig EV1A) and strains were not sensitive to the microtubule drug benomyl, suggesting that SAC functionality was maintained (Fig EV1B).

The mean SAC mRNA numbers per cell, determined by single-molecule mRNA fluorescence *in situ* hybridization (FISH) with probes targeting GFP, were in the range of 3 to 4, even lower than the means of 4.5 to 6 that we had previously observed (Fig 1C,D; EV1C) (Heinrich *et al.*, 2013). This indicates that the traditional tagging strategy indeed influenced gene expression. To test whether expression in the new strains resembles endogenous expression, we used FISH probes against endogenous *mad1*$^{+}$ and *mad2*$^{+}$ and compared strains expressing the endogenous untagged gene with strains expressing the GFP-tagged gene. For *mad2*$^{+}$, the mean mRNA number for untagged and tagged *mad2*$^{+}$ was comparable (Fig 1E). However, untagged *mad1*$^{+}$ showed even fewer mRNA molecules than *mad1*-GFP (Fig 1E), suggesting that the mere addition of GFP, without any changes in the UTRs or surrounding sequences can change expression of *mad1*$^{+}$. [Note that for *mad2*$^{+}$, the efficiency of the gene-specific probe was slightly lower than the GFP probe (Fig EV1D, both probes measured on *mad2*$^{+}$-GFP), but this is not expected to influence the

conclusion in an experiment that only uses the gene-specific probe (Fig 1E).]

While the mean mRNA numbers per cell for the GFP tagged genes were in the range of 3 to 4, the numbers in single cells ranged from 0 to around 9 (Fig 1D,E). As expected (Padovan-Merhar *et al*, 2015; Sun *et al*, 2020; Zhurinsky *et al*, 2010), smaller cells had on average lower numbers than larger cells (Fig EV1E). However, even cells of the same size could differ in mRNA number by 8 or more (Fig EV1E). The spread of mRNA numbers in the cell population was well approximated by a Poisson distribution (Fig 1D,E). A Poisson distribution is expected from constitutive expression, where mRNA is synthesized and degraded in uncorrelated events but with a uniform probability over time. In contrast, "bursty" expression (characterized by alterations of promoter activity and inactivity) would result in an even wider distribution (Zenklusen *et al*, 2008). These results therefore indicate that SAC mRNA numbers vary considerably, but that this variation is within the expected range for constitutive expression.

Mad1⁺ and *mad2⁺* mRNAs do not co-localize in the cytoplasm

The mRNA FISH data also provides the location of mRNAs. Recent work has suggested that co-translational assembly of protein complexes is more prevalent than previously thought (Schwarz & Beck, 2019). How the stable Mad1/Mad2 complex assembles is unknown. When heterodimeric complexes assemble while both subunits are being translated, their mRNAs will co-localize (Panasenko *et al*, 2019). We asked whether this is the case for Mad1 and Mad2. We stained *mad1⁺* mRNA (using a *mad1⁺* probe) and *mad2⁺*-GFP mRNA (using a GFP probe) in the same cells, where both were expressed from their respective endogenous locus. While a *mad1-GFP* strain, used as positive control, showed strong co-localization of the *mad1⁺* and *GFP* probes, there was no evidence for co-localization of *mad1⁺* and *mad2⁺-GFP* mRNA (Fig 1F). This absence of mRNA co-localization excludes that the Mad1/Mad2 complex forms by synchronous co-translational assembly. We will discuss other possibilities below.

Low protein noise can be explained through long protein and short mRNA half-lives

To analyze if and to what extent the strong mRNA variation propagates to the protein level, we quantified GFP-tagged Mad1, Mad2 and Mad3 in single cells using our 'Pomegranate' image analysis pipeline, which allows for 3D segmentation (Fig S1, S2A) (Baybay *et al*, 2020). To subtract autofluorescence, we mixed the GFP-expressing cells with cells not expressing GFP (Fig S1). Unlike for the mRNA, we observed little cell-to-cell variability in the SAC protein concentrations (Fig 2A). As a comparison we imaged a 'noisy' *S. pombe* protein, Nmt1 (Saint *et al*, 2019), which indeed showed pronounced cell-to-cell variability (Fig 2A, S1C). A measure of variability is the coefficient of variation (CV; standard deviation divided by mean). The CVs for Mad1-, Mad2- or Mad3-GFP were in the range of 0.2, whereas that for Nmt1-GFP was around 0.6 (Fig 2A).

This raised the question how the protein concentrations of Mad1, Mad2 and Mad3 can be homogeneous across the population when the mRNA numbers are highly variable. We considered a simple gene expression model with a constitutively active promoter and different mRNA and protein synthesis and degradation rates (see Methods for details) that would all yield mRNA and protein numbers similar to those that we observe for *mad1⁺*, *mad2⁺* and *mad3⁺*. The longer the mRNA half-life, the longer a state of low or high mRNA numbers persists; and the shorter the protein half-life, the more closely protein concentrations follow the mRNA numbers (Fig 2B). Hence long mRNA half-lives and short protein half-lives favour noise, whereas short mRNA-half lives and long protein-half-lives suppress noise (Fig 2B,C; S2B). In the latter case, the long persistence time of proteins buffers fast fluctuations at the mRNA level (Fig 2B).

To ascertain whether this prediction is met by SAC genes, we measured mRNA and protein half-lives. We determined mRNA half-life by metabolic labelling followed by depletion of the labelled pool and quantification of the remaining pool by quantitative PCR. The mRNA half-lives for *mad1⁺*, *mad2⁺* and *mad3⁺* were all in the range of a few minutes (*mad1⁺*: 5.6 min, *mad2⁺*: 7.7 min, *mad3⁺*: 5.2 min) (Fig 2D). This was consistent with the half-lives determined for these genes in a large-scale study using metabolic labelling (Fig S2D) (Eser *et al*, 2016). RNA half-lives have been notoriously difficult to measure, with much variability between studies (Carneiro *et al*, 2019). An

earlier *S. pombe* study (Hasan *et al*, 2014) found longer half-lives across the entire transcriptome, but even in this study SAC genes were at the lower end of mRNA half-lives (Fig S2D). As controls, we measured two unrelated genes with reportedly long and short half-life (Eser *et al.*, 2016), *act1*$^{+}$ and *ecm33*$^{+}$, which behaved as expected (Fig 2D). We determined protein half-lives by translation shut-off using cycloheximide, followed by immunoblotting. The half-lives of Mad1, Mad2 and Mad3 were in the range of many hours, considerably longer than the typical *S. pombe* cell cycle of 2.5 hours (Fig 2E; S2E) and broadly consistent with previous data (Christiano *et al*, 2014; Horikoshi *et al*, 2013; Sczaniecka *et al*, 2008). This large difference in mRNA and protein half-lives explains the low cell-to-cell variability in protein concentration despite the considerable variation in mRNA numbers (Fig 2C). The short mRNA half-life is therefore important to mitigate the effect of the large variation in mRNA numbers.

Mad2^{+} and *mad3*$^{+}$ have low codon stabilization coefficients

One of the determining factors for mRNA half-life is codon optimality, which positively correlates with mRNA stability in several eukaryotes (Hanson & Coller, 2018; Narula *et al*, 2019; Presnyak *et al*, 2015; Wu *et al*, 2019). The codon stabilization coefficient (CSC) describes the correlation between the occurrence of a codon in mRNA transcripts and experimentally determined mRNA stability (Presnyak *et al.*, 2015). The CSC for a codon is positive if this codon is over-represented in stable mRNAs and negative if over-represented in unstable mRNAs. Similar to Harigaya and Parker (Harigaya & Parker, 2016), we determined CSC values for *S. pombe* based on large-scale mRNA half-life measurements (Eser *et al.*, 2016; Hasan *et al.*, 2014). The CSC value for each gene (CSC_g) is the arithmetic mean of the CSC values of all codons in that gene. As had been seen before (Harigaya & Parker, 2016; Presnyak *et al.*, 2015), the CSC_g correlated with other measures of codon optimality such as the percentage of optimal codons or the tRNA adaptation index (tAI) (Fig S3A). Since the SAC genes had short mRNA half-lives, we expected them to have low CSC_g values. Indeed, *mad2*$^{+}$ and *mad3*$^{+}$ were among the 20 % of protein-coding genes with the lowest CSC_g values (Fig 3A,B). This result was independent of which large-scale mRNA half-life data or

182 which correlation parameter was used (Fig S3C,D). These results raise the interesting possibility
183 that codon usage in *mad2*$^+$ and *mad3*$^+$ contributes to their short mRNA half-life. The *mad1*$^+$ gene
184 showed different characteristics, which we will discuss below.

185 **Codon-optimization increases the mRNA concentration of *mad2*$^+$ and *mad3*$^+$**

186 To test if codon usage contributes to the short mRNA half-lives, we codon-optimized *mad2* and
187 *mad3* and inserted the codon-optimized sequence at the respective endogenous locus (Fig 3C;
188 S3B,F). The GFP tag, which remained unchanged, mitigated but did not abolish the effect of the
189 codon optimization on the CSC_g value of the fusion genes (Fig S3B). An increase in mRNA half-
190 life should result in an increased steady-state mRNA number if synthesis was unchanged. Indeed,
191 we found an increased mRNA number for codon-optimized *mad2* and *mad3* compared to the wild-
192 type gene (Fig 3D). Cytoplasmic mRNAs showed a 27 % increase (Fig EV3). For *mad2*$^+$, the
193 increase was restricted to the cytoplasm and not observed in the nucleus, strongly suggesting
194 stabilization of the mRNA (Fig EV3).

195 In *S. cerevisiae*, the RNA helicase Dhh1 (*S. pombe* Ste13) is involved in specifically lowering
196 the mRNA half-life of genes with a high fraction of non-optimal codons (Buschauer *et al*, 2020;
197 Cheng *et al*, 2017; Radhakrishnan *et al*, 2016; Webster *et al*, 2018). Consistently, we observed that
198 deletion of *ste13*$^+$ significantly increased *mad2*$^+$ and *mad3*$^+$ mRNA half-lives—from about 8 min to
199 14 min for *mad2*$^+$, and 5 min to 10 min for *mad3*$^+$ (Fig 3E, EV2C). This indicates that *mad2*$^+$ and
200 *mad3*$^+$ mRNA are subject to Ste13-mediated degradation. The steady-state mRNA numbers were
201 not greatly affected by *ste13*$^+$ deletion (Fig 3D, EV2B, EV3). This is consistent with a global
202 'buffering' of mRNA concentrations that has been observed in budding yeast when mRNA
203 degradation rates or synthesis rates are globally reduced (Fischer *et al*, 2020; Haimovich *et al*,
204 2013; Sun *et al*, 2013; Timmers & Tora, 2018). Buffering has been found to be a global
205 phenomenon, not observed when the mRNA of single genes is stabilized (Garcia-Martinez *et al*,
206 2021). This may explain why mRNA numbers increased after codon-optimization, but not after
207 *ste13*$^+$ deletion. Overall, our results support the hypothesis that non-optimal codons in *mad2*$^+$ and

mad3⁺ contribute to the short mRNA half-life of these genes.

Codon-optimization, but not *ste13⁺* deletion, increases the protein concentration of Mad2 and Mad3

To ask whether the consequences of codon-optimization propagate to the protein level, we quantified Mad2- and Mad3-GFP protein expressed from the wild-type or codon-optimized genes. Both immunoblotting and fluorescence microscopy showed an increase in protein concentration after codon-optimization (Fig 4), which can partly be explained by the increase in mRNA (Fig 3) and might be enhanced by an increased translation efficiency. In contrast, the Mad2 and Mad3 protein concentrations in *ste13Δ* cells remained largely stable when analyzed by immunoblotting (Fig 4B,C), consistent with the RNA results (Fig 3D). Altogether, these data support that codon usage bias towards non-optimal codons in *mad2⁺* and *mad3⁺* lowers their protein concentration but supports a short mRNA half-life, thereby establishing a gene expression pattern that lowers cell-to-cell variability.

Mad1⁺* expression regulation differs from that of *mad2⁺* and *mad3⁺

The *mad1⁺* gene shares a short mRNA half-life with *mad2⁺* and *mad3⁺* (Fig 2D). Different from *mad2⁺* and *mad3⁺*, though, *mad1⁺* has a higher fraction of optimal codons and a CSC_g value above the median of all protein-coding *S. pombe* genes (Fig 3A,B; S3A,B). This was surprising because we expected similar features within the SAC network. Unlike for *mad2⁺* and *mad3⁺*, the *mad1* mRNA number did not increase after codon-optimization, but rather decreased slightly (Fig 5A,B; EV5). A second codon-optimized *mad1* whose sequence was considerably different from the first (77% nucleotide identity; Fig S3F; Table S3) showed the same trend (Fig EV4A, EV5). Similar to *mad2⁺* and *mad3⁺, mad1⁺* mRNA half-life was still prolonged in *ste13Δ* cells (from 6 min to 10 min; Fig 5C), but unlike for *mad2⁺* and *mad3⁺* not reaching statistical significance (Fig EV4E). Thus, the short *mad1⁺* mRNA half-life is less dependent on codon usage bias and Ste13, and hence, different modes of regulation bring about the short mRNA half-life of these SAC genes.

The *ecm33*$^{+}$ control mRNA was strongly stabilized in *ste13*-deleted cells (Fig 5C, EV4E), despite a high fraction of optimal codons in *ecm33*$^{+}$ (Fig 5D). This highlights that—despite some overall correlation—the relationships between codon-optimality, mRNA half-life, and susceptibility to *ste13*$^{+}$ deletion are far from predictable (Fig EV4F) (He *et al*, 2018). It is worth noting that Ecm33 is a membrane-binding protein, which, extrapolating from work in other organisms (Jungfleisch *et al*, 2017; Weber *et al*, 2020), may explain the Ste13-mediated mRNA destabilization.

Codon-optimization of *mad1*$^{+}$ decreases its protein concentration

Unlike Mad2- and Mad3-GFP, whose protein concentration increased after codon optimization, that of Mad1-GFP decreased, both by immunoblotting and fluorescence microscopy (Fig 6). Mad1 protein formed from the codon-optimized mRNA had a similar stability to that formed from wild-type mRNA (Fig S4A,B), and still bound Mad2 (Fig S4C). The reduction, rather than increase, in protein concentration after codon-optimization of *mad1*$^{+}$ corroborates that the codon usage pattern of *mad1*$^{+}$ serves a different purpose than that of *mad2*$^{+}$ and *mad3*$^{+}$. Deletion of *ste13*$^{+}$ had hardly any influence on the Mad1 protein concentration (Fig 6B,C), consistent with the largely unchanged mRNA concentration (Fig 5B).

We previously found that SAC function was well preserved when Mad1 levels were lowered to 30 % (Heinrich *et al.*, 2013). Consistently, we did not observe an obvious growth defect when cells expressing codon-optimized *mad1* were grown in presence of the microtubule-drug benomyl (Fig EV1B), and we did not observe a SAC defect in a live-cell imaging assay where microtubules were depolymerized (Fig S4D,E). To test SAC function in a more sensitive assay, we deleted the gene for the microtubule-interacting protein Alp7 (Sato *et al*, 2003). This also activates the SAC, but less robustly than microtubule-depolymerization. Using this assay, cells expressing codon-optimized *mad1* tended to exit mitosis more quickly than cells expressing wild-type *mad1*$^{+}$ (Fig 6F, S4F). The difference did not reach the level of statistical significance but was reproducible with independent strains. This suggests that synonymous codon changes, without any change in the protein sequence, can impair SAC function.

Upstream and downstream sequences of *mad1⁺* are insufficient for proper expression

The lower mRNA concentrationa after *mad1* codon-optimization (Fig 5B, EV4A) suggested that the concentration of *mad1⁺* mRNA is not purely determined by regulatory sequences upstream and downstream of the coding sequence. This is supported by our observation that merely fusing GFP to *mad1⁺*, without altering surrounding sequences, increases its mRNA number (Fig 1E). Further supporting this notion, but rather surprisingly, we found that replacing the *mad1⁺* coding sequence with GFP produced neither significant amounts of mRNA nor protein (Fig S5A,B). This again contrasted with the *mad2⁺* and *mad3⁺* genes, which produced comparable amounts of mRNA and protein when the original coding sequence was replaced with GFP (Fig S5C,D). Hence, the sequences surrounding the *mad1⁺* coding sequence are insufficient to establish *mad1⁺*-like expression, and contributions from the coding sequence are required. Preserving the first 66 or 108 base pairs of *mad1⁺* partly rescued both mRNA and protein levels but not completely (Fig S5A,B). While this suggests that the 5' region of the *mad1⁺* coding sequence carries signals that are important for mRNA synthesis or stabilization, some other genes contain sequences that can compensate. Introducing an *nmt1⁺*-GFP fusion gene or fusions between *S. cerevisiae* GCN4 and N-terminally truncated versions of *S. pombe mad1⁺* (Heinrich *et al*, 2014) allowed for expression from the *mad1⁺* locus (Fig S5A,B). What these genes share, that GFP does not, remains unclear.

Altogether, these results indicate that *mad1⁺* expression has some unique aspects: *mad1⁺* uses a different mode for reducing mRNA half-life than *mad2⁺* or *mad3⁺*, and its coding sequence carries elements that help transcribe, stabilize or translate RNA.

Mad1 homodimers assemble co-translationally

We considered whether *mad1* may have a certain codon usage pattern to facilitate protein production or complex formation (Liu *et al*, 2021). Mad1 forms a homodimer through a long N-terminal coiled-coil (Piano *et al.*, 2021; Sironi *et al.*, 2002), but—except in a very recent genome-wide study (Bertolini *et al*, 2021)—how this homodimer forms has not been examined. If formation was co-translational rather than post-translational, this may require a certain pattern of codon

usage for proper complex formation. To assess dimer formation, we examined cells expressing both tagged and untagged Mad1. If Mad1 dimer formation was post-translational, it should be possible to observe interactions between tagged and untagged Mad1. However, in haploid strains expressing a C-terminally GFP-tagged and an untagged *mad1⁺* gene, a GFP immunoprecipitation almost exclusively precipitated Mad1-GFP, but not untagged Mad1 (Fig 7A). In contrast, a Mad1 immunoprecipitation precipitated Mad1-GFP and Mad1 in approximately the same ratio in which they were present in the extract. These experiments used a monomeric version of GFP. Thus, it is unlikely that this pattern is driven by dimerization of GFP. With two versions of Mad1 being expressed, a slight bias towards the form that is being pulled down would be expected even when heterodimers between these forms were generated with equal likelihood as homodimers (Fig EV6A). At a 1:1 ratio of the isoforms in the extract, a 2:1 ratio would be expected in an immunoprecipitation or pull-down. However, the bias that we observed always exceeded the expected bias, usually vastly (Fig 7, EV6). Hence, we propose that Mad1 forms homodimers between isoforms more efficiently than heterodimers. This is most easily explained by co-translational assembly of Mad1 dimers from the nascent chains of two ribosomes translating *mad1⁺* from the same mRNA molecule (Fig 7B).

We further corroborated this finding by using diploid strains expressing Mad1-GFP and Mad1-Strep from the two endogenous loci. Again, a GFP-immunoprecipitation isolated Mad1-GFP but very little Mad1-Strep, whereas a Strep pull-down isolated Mad1-Strep but very little Mad1-GFP (Fig 7C, EV6B). We obtained similar results after *in vitro* translation of Mad1 (Fig EV6C): when Mad1-GFP and Mad1-flag-His were co-translated in a rabbit reticulocyte lysate, a subsequent GFP immunoprecipitation isolated very little Mad1-flag-His, and a His-pull-down isolated very little Mad1-GFP. Heterodimerization between C-terminal Mad1 fragments has previously been reported in an *in vitro* translation (Kim *et al.*, 2012). However, in our experiments, even C-terminal fragments showed a strong bias towards the form that was being precipitated, both in yeast extracts and after *in vitro* translation (Fig S6). To exclude that heterodimer formation between Mad1-GFP and untagged Mad1 was unphysiologically prevented by the large GFP tag, we tested a combination of

Mad1-flag-His and untagged Mad1 in an *in vitro* translation. Again, His pull-down almost exclusively isolated Mad1-flag-His, whereas a Mad1 immunoprecipitation isolated both forms in approximately the same ratio in which they were present in the extract (Fig 7D).

To further test the idea that Mad1 dimer assembly occurs on a single mRNA molecule (Fig 7B), we examined *mad1* mRNA. Consistent with few heterodimers on the protein level, we did not observe colocalization between two different *mad1* isoform mRNAs present in the same cell (Fig 7E). Intensity measurements of mRNA FISH spots suggested the presence of single mRNAs, not mRNA doublets, when both untagged *mad1⁺* and *mad1⁺*-GFP were expressed (Fig 7E, left; EV6D). Further supporting this finding, the number of mRNA spots for a given isoform was identical in the absence or presence of another isoform (Fig 7E, right), indicating that the isoforms do not co-localize. We additionally tested the possibility that mRNAs of the same isoform may co-localize by comparing FISH spot intensities with probes against GFP between *mad1⁺*-GFP mRNA and *mad3⁺*-GFP mRNA (the latter coding for Mad3 monomers). We did not find any difference in spot intensity (Fig 7F). Hence, we conclude that *mad1⁺* mRNAs rarely, if ever, co-localize, and we favour the idea that Mad1 homodimers emerge from two ribosomes co-translating a single mRNA (Fig 7B).

The fact that Mad1 homodimers form co-translationally is consistent with the idea that synonymous codon changes may subtly impair complex formation and therefore translation efficiency and mRNA stability. Overall, these results suggest that codon usage bias within *mad1⁺* contributes to maintaining proper mRNA and protein levels, possibly by supporting Mad1 folding and dimerization.

Discussion

Proteins are the workhorses of cells. The deployment of this workhorse army is controlled by regulatory elements encoded in DNA that are still incompletely understood. The spindle assembly checkpoint is sensitive to expression changes, and we therefore asked which features of gene expression may be important for its proper function. Our results suggest that a combination of short mRNA half-lives and long protein half-lives is important to keep protein variability low. We also find

that—despite their closely shared function—*mad1⁺* differs in its expression features from *mad2⁺* and *mad3⁺*. The coding sequences of *mad2⁺* and *mad3⁺* contribute to the short mRNA half-life of these genes, whereas that of *mad1⁺* contributes to maintaining mRNA (Fig S5) and protein levels (Fig 6). We propose that the choice of synonymous codons in *mad1⁺* is optimized for the formation of the Mad1 homodimer and, ultimately, the Mad1/Mad2 complex.

Short mRNA half-life of constitutively expressed SAC genes favours low noise

The short mRNA half-lives of *mad1⁺*, *mad2⁺* and *mad3⁺*, along with their long protein half-lives, can explain the low protein noise of SAC genes despite low and variable mRNA numbers (Fig 1,2) (Thattai & van Oudenaarden, 2001). In human cells, a long protein half-life has also been shown to buffer the effects of variable mRNA numbers (Raj *et al*, 2006). Human Mad1, Mad2 and BubR1 (Mad3 ortholog) are also highly stable proteins (Rodriguez-Bravo *et al*, 2014; Schweizer *et al*, 2013; Suijkerbuijk *et al*, 2010; Varetti *et al*, 2011), which will support stable protein concentrations over time and between cells. SAC genes are certainly not unique in combining a short mRNA and long protein half-life to achieve low noise. Other constitutively expressed genes that produce low or modest amounts of protein will likely show a similar behavior. Keeping noise low in this manner requires a high turn-over of mRNA that confers some energy cost. An alternative way to keep protein noise low would be to produce the same amount of protein from a larger number of more stable mRNA molecules (Fig S2C). Several side-effects likely prohibit this solution as a general strategy. For example, the cytoplasm would be much more crowded with mRNAs, and stable mRNAs may accumulate chemical damage. Indeed, genes using an expression strategy of high transcription and low translation rates are exceedingly rare among different eukaryotes (Hausser *et al*, 2019).

Different SAC genes employ different strategies for achieving short mRNA half-life

The half-life of an mRNA is influenced by sequence motifs, codon usage and other factors that influence translation. Currently, known factors predict around 50–60% of mRNA half-life in budding

yeast (Cheng *et al.*, 2017; Neymotin *et al*, 2016). At least two elements seem to play a role for *mad2+* and *mad3+*: our data suggest that the mRNA half-lives are shortened by a high fraction of non-optimal codons (Fig 3); in addition, the *mad2+* and *mad3+* 3' UTRs contain sequence motifs that are associated with a short mRNA half-life (Eser *et al.*, 2016). We previously found higher mRNA numbers after traditional tagging, which changed the 3' UTR to that of a highly expressed gene (Heinrich *et al.*, 2013), suggesting that the predicted motifs in the 3' UTR may indeed be functional. For *mad1+*, in contrast, overall codon usage bias seems to play a lesser role (Fig 5), and the *mad1+* 3' UTR does not contain reported motifs implicated in half-life shortening (Eser *et al.*, 2016). We suspect that other elements that influence translation efficiency may be important. Generally, less efficiently translated mRNAs are less stable (Hanson & Coller, 2018), and *mad1+* seems to be translated less efficiently than *mad2+* or *mad3+* (Rubio *et al*, 2020).

Formation of the Mad1/Mad2 complex involves co-translation assembly of the Mad1 dimer but not synchronous assembly of the tetramer

Mad1 and Mad2 form a tight tetrameric complex (Kim *et al.*, 2012; Sironi *et al.*, 2002), but how this complex assembles is unknown. Our experiments suggest that the Mad1 homodimer forms between two polypeptides translated from the same mRNA, and that Mad1 molecules translated from different mRNA molecules associate very inefficiently with each other, if at all (Fig 7). This assembly mode is further supported by a recent proteome-wide analysis in human cells that came to the same conclusion for Mad1 and other proteins with N-terminal dimerization through a coiled-coil (Bertolini *et al.*, 2021). At least two studies have expressed Mad1 N-terminal fragments and full-length Mad1 from two different loci and have interpreted the failure to see association between those two as an inability of the N-terminal fragment to dimerize (Ji *et al*, 2018; Jin *et al*, 1998). However, we suggest that the capacity of an N-terminal Mad1 fragment to dimerize would need to be based on assessing self-association rather than assessing association with Mad1 expressed from a different locus. Of note, C-terminal Mad1 fragments also dimerize, possibly post-translationally (Kim *et al.*, 2012), although our own experiments still suggest a preference of

389 homodimerization (Fig S6).

390 While we propose that assembly of the Mad1 homodimer occurs co-translationally, the
391 assembly of the Mad1/Mad2 tetramer does not occur in synchronous co-translational fashion, since
392 the mRNAs for *mad1⁺* and *mad2⁺* do not co-localize in the cytoplasm (Fig 1). This leaves open the
393 possibility of post-translational assembly of the tetramer or of asynchronous co-translational
394 assembly, where one protein is already fully formed and binds the other that is being translated
395 (Duncan & Mata, 2011; Shiber *et al*, 2018). Formation of the C-Mad2/Cdc20 complex necessitates
396 catalysis (Faesen *et al*, 2017; Kulukian *et al*, 2009; Lad *et al*, 2009; Piano *et al*., 2021; Simonetta
397 *et al*, 2009), making it likely that C-Mad2/Mad1 formation also needs to be facilitated. We favour
398 the idea that the tetramer assembles while one of the proteins is being translated, and it will be
399 interesting to test whether the *mad1⁺* mRNA binds Mad2 protein or vice versa to facilitate such an
400 assembly. It will also be interesting to examine whether different eukaryotes use the same
401 assembly pathway for the highly conserved Mad1/Mad2 complex.

402 **Potential SAC malfunction from synonymous mutations**

403 Overall, our data suggest that the coding sequences of *mad1⁺*, *mad2⁺* and *mad3⁺* modulate
404 gene expression. Hence, even synonymous mutations carry some risk of impairing the SAC. We
405 suspect that *mad1* is most susceptible to single synonymous substitutions, given the need for co-
406 translational homodimer assembly (Fig 7), which may be facilitated by controlling the speed of
407 ribosome movement (Liu *et al*., 2021). In *S. pombe*, a cluster of non-optimal codons follows the
408 coiled-coil region of *mad1⁺* (Fig S3E, S7), which may ensure that the N-terminal coiled-coil is fully
409 formed before the remainder of Mad1 is translated.

410 It will be interesting to test whether synonymous mutations found in cancer samples can
411 modulate SAC gene expression or function. Within MAD2L1 (*H.s. mad2*), synonymous mutations
412 detected in cancer samples seem to cluster in a conserved region with high CSC values preceding
413 the 'seat belt' (Fig S7), suggesting that codon usage bias in this region may be functionally
414 important. Although most synonymous mutations will only have small effects, they may fuel

carcinogenesis. This is particularly true in the context of the SAC, because drastic impairment is more likely to be detrimental for cancer cells whereas subtle impairment may promote carcinogenesis (Cohen-Sharir *et al.*, 2021; Funk *et al.*, 2016; Kops *et al.*, 2004; Quinton *et al.*, 2021). The role of synonymous mutations and changes in tRNA expression in cancer is more and more recognized (Sauna & Kimchi-Sarfaty, 2011; Supek *et al*, 2014). Our data suggest that the SAC may be no exception.

421 ## Reagents and Tools

Reagent/Resource	Reference or Source	Identifier or Catalog Number
Experimental Models		
Schizosaccharomyces pombe strains	This study	Table S1
Saccharomyces cerevisiae strain	Nick Buchler, NC State University, USA	Table S1
Recombinant DNA Indicate species for genes and proteins when appropriate		
sgRNA sequences	This study	Table S2
Codon-optimized *mad1*, *mad2*, and *mad3*	This study	Table S3
PCR fragments for *in vitro* transcription	This study	Table S6
Antibodies		
Mouse anti-Cdc13 (monoclonal)	Novus	Cat # NB200-576; RRID: AB_10003103
Rabbit anti-Cdc2 (polyclonal)	Santa-Cruz	Cat # sc-53; RRID: AB_2074908
Mouse anti-GFP (mix of 2 monoclonals)	Roche	Cat # 11814460001; RRID: AB_390913
Rabbit anti-Mad1 (polyclonal, against peptide ADSPRDPFQSRSQLC)	Heinrich et al., 2013, PMID: 24161933	N/A
Rabbit anti-Mad2 (polyclonal, against recombinant protein)	Sewart et al., 2017, PMID: 28366743	N/A
Rabbit anti-Mad3 (polyclonal, against recombinant protein)	Sewart et al., 2017, PMID: 28366743	N/A
Rabbit anti-Strep-tag II (monoclonal, recombinant)	Abcam	Cat # ab180957
Rabbit anti-Strep-tag II (polyclonal)	Abcam	Cat # ab76949; RRID: AB_1524455
Mouse anti-tubulin	Sigma	Cat # T5168; RRID: AB_477579
Goat anti-mouse HRP	Jackson ImmunoResearch Labs	Cat # 115-035-003; RRID: AB_10015289
Goat anti-rabbit HRP	Jackson ImmunoResearch Labs	Cat # 111-035-003; RRID: AB_2313567
Oligonucleotides and other sequence-based reagents		
FISH probes	This study	Table S4
qPCR primers	This study	Table S5
Chemicals, Enzymes and other		

reagents		
Cycloheximide (from *Streptomyces griseus*)	Chem Impex	Cat # 00083
Wizard SV Gel and PCR Clean-Up System	Promega	Cat # A9285
SuperScript IV First Strand Synthesis System	ThermoFisher	Cat # 18091050
HiScribe T7 ARCA mRNA Kit (with tailing)	New England Biolabs	Cat # E2060S
Monarch RNA Cleanup Kit	New England Biolabs	Cat # T2040S
Rabbit Reticulocyte Lysate, Nuclease-Treated	Promega	Cat # L4960
EasyTag EXPRESS 35S Protein Labeling Mix	Perkin Elmer	Cat # NEG772007MC
SUPERase•In RNase Inhibitor	ThermoFisher	Cat # ACM2694
SuperSignal West Pico PLUS Chemiluminescent Substrate	ThermoFisher	Cat # 34580
cOmplete, EDTA-free Protease Inhibitor Cocktail	Roche	Cat # 04693132001
Halt Protease Inhibitor Cocktail, EDTA-Free (100X)	ThermoFisher	Cat # 87785
PhosSTOP	Roche	Cat # 04906837001
Halt Phosphatase Inhibitor Cocktail	ThermoFisher	Cat # 78420
Dynabeads Protein G	ThermoFisher	Cat # 10003D
Dynabeads His-Tag Isolation and Pulldown	ThermoFisher	Cat # 10103D
MagStrep "type3" XT beads	IBA Lifesciences	Cat # 2-4090-002
Pierce BCA Protein Assay Kit	ThermoFisher	Cat # 23225
EMM (Edinburgh's Minimal Medium)	MP Biomedicals	Cat # 114110022
Lectin	Sigma	Cat # L1395
Software		
Fiji/ImageJ	Schindelin et al., 2012, PMID: 22743772	https://imagej.net/Using_Fiji; RRID: SCR_002285
SoftWoRx	Applied Precision, GE Healthcare	http://incelldownload.gehealthcare.com/bin/download_data/SoftWoRx/6.5.2/SoftWoRx.html; RRID: SCR_019157
MetaMorph	Molecular Devices	Version 7.10.1

YeaZ	Dietler et al., 2020, PMID: 33184262	N/A
ImageLab	Bio-Rad Laboratories	Version 6.0.1 build 34
Matlab	Mathworks	https://www.mathworks.com; RRID: SCR_001622
FISH-Quant	Mueller et al., 2013, PMID: 23538861	N/A
Trainable Weka Segmentation	Arganda-Carreras et al., 2017, PMID: 28369169	N/A
Prism 9	GraphPad Software, Inc	https://www.graphpad.com; RRID: SCR_002798
R	Cran.R	https://cran.r-project.org; RRID: SCR_001905
R studio	N/A	https://www.rstudio.com; RRID: SCR_000432
tidyverse package	Cran.R	https://tidyverse.tidyverse.org; RRID: SCR_019186, Version 1.3.1
ggplot2 package	Cran.R	https://ggplot2.tidyverse.org/; RRID: SCR_014601
alphashape3d package	Cran.R	https://CRAN.R-project.org/package=alphashape3d, Version 1.3.1
boxcoxmix package	Cran.R	https://CRAN.R-project.org/package=boxcoxmix, Version 0.28
broom package	Cran.R	https://CRAN.R-project.org/package=broom, Version 0.7.9
broom.mixed package	Cran.R	https://CRAN.R-project.org/package=broom.mixed, Version 0.2.7
Cairo package	Cran.R	https://CRAN.R-project.org/package=Cairo, Version 1.5-12.2
cowplot package	Cran.R	https://CRAN.R-project.org/package=cowplot; RRID: SCR_018081, Version 1.1.1
DescTools package	Cran.R	https://cran.r-project.org/package=

		DescTools, Version 0.99.43
egg package	Cran.R	https://CRAN.R-project.org/package=egg, Version 0.4.5
geometry package	Cran.R	https://CRAN.R-project.org/package=geometry, Version 0.4.5
gridExtra package	Cran.R	https://CRAN.R-project.org/package=gridExtra, Version 2.3
lemon package	Cran.R	https://CRAN.R-project.org/package=lemon, Version 0.4.5
lme4 package	Cran.R	https://cran.r-project.org/web/packages/lme4/index.html; RRID: SCR_015654
Irescale package	Cran.R	https://CRAN.R-project.org/package=Irescale, Version 2.3.0
MASS package	Cran.R	https://CRAN.R-project.org/package=MASS; RRID: SCR_019125
mclust package	Cran.R	https://cran.r-project.org/package=mclust
nabor package	Cran.R	https://cran.r-project.org/package=nabor
pbkrtest package	Cran.R	https://cran.r-project.org/package=pbkrtest
plotly package	Cran.R	https://plot.ly; RRID: SCR_013991, Version 4.10.0
plyr package	Cran.R	https://cran.r-project.org/package=plyr
readxl package	Cran.R	https://cran.r-project.org/web/packages/readxl/index.html; RRID: SCR_018083, Version 1.3.1
rgl package	Cran.R	https://CRAN.R-project.org/package=rgl, Version 0.107.14
sf package	Cran.R	https://CRAN.R-project.org/package=

		sf
shotGroups package	Cran.R	https://CRAN.R-project.org/package=shotGroups, Version 0.8.1
spatstat package	Cran.R	https://cran.r-project.org/package=spatstat
Other		
Mixer mill MM400	Retsch	Cat # 20.745.0001
Grinding jar 10 mL	Retsch	Cat # 01.462.0236
Grinding jar 25 mL	Retsch	Cat # 01.462.0213
Adapter for reaction vials	Retsch	Cat # 22.008.0008
Glass beads, acid-washed	Sigma	Cat # G8772
μ-Slide 8-well, glass bottom	Ibidi	Cat # 80827
Y04C Microfluidic Plate for Haploid Yeast	CellAsic / Sigma	Cat # Y04C-02-5PK
Invitrogen NuPAGE 4 to 12 %, Bis-Tris, 20-well	Invitrogen	Cat # WG1402BOX
Invitrogen NuPAGE 4 to 12 %, Bis-Tris, 20-well	Invitrogen	Cat # NP0322BOX
Immobilon-P PVDF membrane	Millipore	Cat # IPVH00010

Methods and Protocols

Yeast strains

Yeast strains are listed in Table S1. Tagging of *nmt1*$^{+}$ and deletion of *ste13*$^{+}$ and *alp7*$^{+}$ were done by conventional PCR-based gene targeting (Bähler *et al*, 1998). Marker-less insertion at the endogenous locus was performed either by replacement of a counter-selectable rpl42-hphNT1 cassette in an rpl42::cyhR(sP56Q) background (Roguev *et al*, 2007) or by using CRISPR/Cas9 (Jacobs *et al.*, 2014). Sequences used for targeting Cas9 are listed in Table S2. The *mad2*$^{+}$*-ymEGFP* strain contains a single, silent (AGG to AGA) PAM site mutation at amino acid position 173 of Mad2. The *mad3*$^{+}$*-ymEGFP* strain contains a single, silent (TTG to TTA) PAM site mutation at amino acid position 199 of Mad3. Yeast, monomeric enhanced GFP (ymEGFP) was derived from

yEGFP (yeast codon optimized green fluorescent protein (Watson *et al*, 2008)) by mutation of Alanine 206 to Arginine (A206R), which is expected to reduce dimerization (Zacharias *et al*, 2002). Codon-optimization used proprietary algorithms by two different companies, and sequences are listed in Table S3. The strain with two differently tagged versions of *mad1⁺* has *mad1⁺-ymEGFP* along with 110 bp upstream and 164 bp downstream of the coding sequence integrated between the *leu1⁺* and *apc10⁺* gene.

Yeast cultures

S. pombe cultures were grown at 30°C either in rich medium (yeast extract supplemented with 0.15 g/L adenine; YEA) or in Edinburgh minimal medium (EMM, MP Biomedicals, 4110012) supplemented with 0.2 g/L leucine, 0.15 g/L adenine or 0.05 g/L uracil if required (Petersen & Russell, 2016). When cultures in minimal medium were started at low concentration, 'pre-conditioned medium' was added to a maximum of 50 %. Pre-conditioned medium was obtained by growing cells in EMM and then removing the cells by filtration. For growth assays, cells were grown in YEA to a concentration of around 1 x 10^7 cells/mL, diluted to 4 x 10^5 cells/mL in YEA and further diluted in a 1:5 dilution series. 10 μL were spotted on indicated plates. *S. cerevisiae* cultures were grown at 30°C in yeast extract supplemented with 20 mg/mL each of Bacto peptone and dextrose (YPD).

Cycloheximide treatment for determination of protein half-lives

Cells were grown in EMM (plus supplements required for auxotrophic mutations) to a final concentration of around 1 x 10^7 cells/mL. Cultures were diluted to 8 x 10^6 cells/mL, transferred to a 30°C water bath for 30 minutes and a sample was taken prior to addition of cycloheximide (CHX) to a final concentration of 1 mg/mL. Cells were collected at specified timepoints, spun down at 980 rcf and frozen in liquid nitrogen before processing.

***In vitro* transcription and translation**

The T7 promoter was appended 5' of the *mad1* transcription start site by PCR. Precise

458 sequences are available in Table S6. Full-length *mad1*$^{+}$ was amplified from cDNA generated using
459 the SuperScript IV First Strand Synthesis System (ThermoFisher). *Mad1* fragments 3' of the intron
460 were amplified from genomic DNA. PCR fragments were purified using the Wizard SV Gel and
461 PCR Clean-Up System (Promega). *In vitro* transcription was carried out with the HiScribe T7 ARCA
462 mRNA Kit (with tailing) (New England Biolabs) using between 25 and 70 ng/μL template DNA.
463 Reactions were run at 32ºC or 37ºC for 2 hours. RNA was purified using the Monarch RNA Cleanup
464 Kit (New England Biolabs). RNAs were mixed and diluted as required before adding them to rabbit
465 reticulocyte lysate (Promega). Translation reactions contained amino acid mix without Methionine,
466 approx. 1 mCi/mL ^{35}S-Methionine/Cysteine mix (Perkin Elmer, NEG772007MC), 0.2 U/μL
467 SUPERase•In RNase Inhibitor (ThermoFisher), and between 0.35 and 40 ng/μL RNA. Incubation
468 was at 30ºC for 1 hr 30 min.

469 **Denatured whole cell extracts**

470 Cells were grown to a final concentration of around 1 x 10^7 cells/mL and collected by
471 centrifugation (1 x 10^8 cells per sample). Supernatant was removed and cells were washed with
472 1 mL of 20 % trichloroacetic acid (TCA). Supernatant was removed and cells were resuspended in
473 500 μL of water. 75 μL of NaOH/beta-mercaptoethanol (final conc. = 0.22 M NaOH, 0.12 M b-ME)
474 was added and samples incubated on ice for 15 minutes. 75 μL of 55 % TCA was added and
475 samples incubated on ice for another 10 minutes. Samples were spun at 16,900 rcf for 10 minutes
476 at 4°C, and supernatant was removed. Pellets were resuspended in 100 μL sample buffer (50 μL
477 of 2x HU buffer [8 M urea, 5% SDS (w/v), 200 mM Tris-HCl pH 6.8 (v/v), 20% glycerol (v/v), 1 mM
478 EDTA (v/v), 0.1% (w/v) bromophenol blue], 40 μL water and 10 μL of 1 M DTT) to a final
479 concentration corresponding to 1 x 10^9 cells/mL. Approximately 150 μL of acid washed beads
480 (Sigma) were added before agitation in a ball mill (Mixer Mill 400; Retsch) for 2 minutes at 30 Hz.
481 Tubes were pierced at the bottom, cell extract was collected from the beads by centrifugation and
482 heated at 75ºC for 5 minutes. Typically, the extract equivalent of 2 – 3 x 10^6 cells was loaded for
483 immunoblotting.

Immunoprecipitation or pull-down from yeast cell extract

Asynchronously growing cultures were harvested, washed with deionized water, or with 20 mM Tris pH 7.5 / 150 mM NaCl, and frozen as droplets in liquid nitrogen. Cell powder was prepared from these droplets using a ball mill (Mixer Mill 400; Retsch) for 30 seconds at 30 Hz under cryogenic conditions. Cell powder was resuspended in lysis buffer (20 mM Tris pH 7.5, 150 mM NaCl, 5% glycerol, 0.1% NP-40) and protein concentration was determined by BCA assay (ThermoFisher). For immunoprecipitations, powder was resuspended to a final concentration of 15–20 mg/mL in lysis buffer supplemented with a 5–10x final concentration of protease inhibitor cocktail and a 1x final concentration of phosphatase inhibitor cocktail. Extracts were spun down for 10 minutes at 4ºC and 16,900 rcf. For the input sample, supernatant was mixed with an equal volume of sample buffer (2x HU buffer with 200 mM DTT, or 2 x NuPAGE LDS sample buffer with 10% beta-mercaptoethanol) and heated for 3–5 minutes at 75ºC. For immunoprecipitations, Protein G Dynabeads (ThermoFisher) were covalently coupled with anti-GFP antibodies (Roche, 160 μg antibody per 1 mL bead suspension) or anti-Mad1 antibodies (80 μg antibody per 1 mL bead suspension). Strep-tag pull-downs used MagStrep "type3" XT beads (IBA Lifesciences). Immunoprecipitations used around 30 μL bead suspension per 200 μL of extract and were performed for 10 minutes at 4ºC on a rotating wheel. Strep pull-downs used around 200 μL bead suspension per 200 μL of extract and were performed for 45 minutes to 1 hour at 4ºC on a rotating wheel. Beads were washed with lysis buffer (IPs), or with a more stringent wash buffer (20 mM Tris pH 7.5, 300 mM NaCl, 5 % glycerol, 1 % NP-40) for some Strep pull-downs. Elution from anti-GFP or anti-Mad1 beads was performed by addition of 7–25 μL 100 mM citric acid and gentle agitation for 5 minutes at 4ºC. Samples were neutralized by addition of 1.5 M Tris pH 9.2, mixed with an equal volume of sample buffer and heated at 75ºC for 3 minutes. Elution from MagStrep beads was performed with sample buffer and incubation at 95ºC for 2 minutes, or 85ºC for 5 minutes.

Immunoprecipitation or pull-down after *in vitro* translation

In vitro translation reactions (IVTs) were diluted to 6–13-times the original volume with either

Tris buffer for immunoprecipitations (final concentration: 20 mM Tris pH 7.5, 150 mM NaCl, 0.1 % NP-40), or with sodium-phosphate buffer for Ni-NTA pull-downs (final concentration: 50 mM sodium-phosphate pH 8.0, 300 mM NaCl, 0.01 % Tween-20). Immunoprecipitations used 10 μL Dynabeads suspension, Ni-NTA pull-downs used 40 μL Ni-NTA Dynabeads suspension per 15 μL original IVT (volume prior to dilution). Immunoprecipitations were processed as above, Ni-NTA beads were washed with sodium-phosphate buffer plus 10–20 mM imidazole and 0.1 % NP-40, and eluted with sodium-phosphate buffer plus an additional 300 mM imidazole.

Immunoblotting

Proteins were separated by SDS-PAGE (NuPAGE, Bis-Tris, MOPS buffer, Thermo Fisher) and transferred onto a PVDF membrane (Immobilon-P, Millipore) in a semi-dry blotting assembly (Amersham Biosciences TE-70 ECL) using transfer buffer (39 mM glycine, 48 mM Tris base) with 10% methanol, 0.01 % SDS, and 1:1,000 NuPAGE Antioxidant. Membranes were probed with mouse anti-GFP (Roche, 11814460001), rabbit anti-Cdc2 (CDK1, Santa Cruz, SC-53), mouse anti-Cdc13 (cyclin B, Novus, NB200-576), rabbit anti-Mad1 (Heinrich *et al.*, 2013), rabbit anti-Mad2 (Heinrich *et al.*, 2013), rabbit anti-Mad3 (Heinrich *et al.*, 2013), rabbit anti-Strep (Abcam, ab180957 and ab76949) or mouse anti-tubulin (Sigma, T5168). Secondary antibodies were either anti-mouse or anti-rabbit conjugated to HRP (Dianova) and quantified by chemiluminescence using SuperSignal West Dura ECL (ThermoFisher) and imaged on a Bio-Rad Gel Doc system. Chemiluminescence signals were quantified on non-saturated images using Image Lab software (Bio-Rad). Measurements from a reference dilution series were used to create a standard curve, which was used to determine the concentration of sample relative to the reference. Membranes with radioactive proteins were dried and exposed to a phosphorscreen (GE Healthcare), which was read-out on a Typhoon phosphorimager (GE Healthcare/Cytiva).

Quantification of GFP fusion proteins in single cells (3D segmentation)

To quantify GFP fusion proteins in single cells, cells were grown in EMM (plus supplements that

were required for auxotrophic mutations) at 30ºC to a final concentration of 6–9 x 10^6 cells/mL. Cultures of GFP-positive and GFP-negative cells were mixed at a 1:1 ratio to a final concentration of 2.5–6.0 x 10^6 cells/mL and incubated for 30 minutes at 30ºC. To ensure a uniform and flat imaging plane, cells were loaded into a Y04C microfluidics trapping plate (Millipore Sigma) and incubated inside a climate-controlled microscope chamber for 2 hours at 30ºC with constant flow of fresh media. Imaging was performed on a DeltaVision Elite system equipped with a PCO edge sCMOS camera and an Olympus 60x/1.42 Plan APO oil objective. Images were acquired for ymEGFP, tdTomato and brightfield as 7.2 μm or 10 μm stacks with images separated by 0.1 μm. The acquired image area was 1024 x 1024 pixels with 1 x 1 binning. All images were deconvolved using SoftWoRx software. To correct for uneven illumination, deconvolved fluorescence images were flatfielded individually for each channel using a custom FIJI script (Baybay *et al.*, 2020).

The Pomegranate image analysis pipeline (Baybay *et al.*, 2020) was used to segment nuclei (using TetR-tdTomato-NLS) and whole cells (using brightfield signal and spherical extrusion of the midplane segmentation) (Fig S1A). We corrected for chromatic aberration and for stretching of distances in the Z direction (Baybay *et al.*, 2020). Further analysis was conducted in R (R-Core-Team, 2020) and figures were produced using the package ggplot2 (Wickham, 2016).

Only information from mono-nucleated cells for which both the whole cell and the nucleus had been segmented was retained. Cells were excluded if one or more of the following conditions were met: the nuclear segmentation protruded beyond the three-dimensional bounds of the cell; whole-cell segmentation was cut-off by more than two slices because insufficient slices in Z had been recorded; cell was at the image edge and incompletely recorded; the nucleus had an aspect ratio (diameter in Z to diameter in XY) of less than 0.8 or more than 1.2; cell volume was in the 0.1st or 99.9th percentile. Cells with or without GFP signal were distinguished by k-means (k = 2) clustering (Fig S1D-F), except for Nmt1-GFP, where the threshold for each image was set manually. One image, where the autofluorescence of GFP-negative cells deviated by more than three standard deviations from that of other images, was excluded. One additional image, where the cells had visibly moved during acquisition, was also excluded.

562 To subtract autofluorescence and other background, we averaged the fluorescence intensity
563 per cell or nuclear volume for GFP-negative cells in an image and subtracted that value from the
564 fluorescence intensity per cell or nuclear volume of each GFP-positive cell in the image. For a rough
565 estimate of absolute concentration in nanomolar, we used our previous estimate of about 70 nM
566 Mad3-GFP in the cell nucleus (Heinrich *et al.*, 2013) and normalized all background-subtracted
567 data to this value.

568 Even after background subtraction, we observed some variation of mean intensities between
569 single images (Fig S1F) and we could not distinguish whether these differences were a
570 consequence of sampling or came from conditions on the microscope stage while recording the
571 image. We therefore opted to determine the coefficient of variation (CV = standard deviation /
572 mean) for each protein not across all images, but instead for each image separately; Fig 2A shows
573 the variation across images.

574 Generalized linear mixed models were used to test for differences in whole-cell GFP
575 concentration between wild-type and codon-optimized Mad1, Mad2, and Mad3 from the single-cell
576 measurements. A separate model was fit for each gene and included whole-cell GFP concentration
577 as the response variable and genotype (wild-type versus codon-optimized) as a categorical fixed
578 effect predictor variable. Two nested random effects variables, experimental replicate and image,
579 were also included in the model (random intercepts only). To meet the model assumptions of
580 normality and constant variance, GFP concentration was transformed with a Box Cox
581 transformation using 'optim.boxcox' from the boxcoxmix package. Wild-type and codon-optimized
582 genotypes were determined to have significantly different GFP concentrations if the 95 % bootstrap
583 confidence interval for the genotype coefficient excluded 0.

584 **Quantification of GFP in single cells (2D segmentation and projection)**

585 For experiments evaluating fluorescence signals after replacing the coding sequences of *mad1*$^{+}$,
586 *mad2*$^{+}$, and *mad3*$^{+}$ (Fig S5), quantification was performed on projections, using 2D segmentation
587 of cells. Cells were grown in minimal medium, collected by centrifugation from liquid cultures,

mounted in medium on a slide, and brightfield and fluorescence images were collected immediately at room temperature. At least two slides were prepared and imaged for each strain. Images were recorded on a Zeiss AxioImager M1, using Xcite Fire LED illumination (Excelitas), a Zeiss Plan-Apochromat 63x/1.40 Oil DIC objective and an ORCA-Flash4.0LT sCMOS camera (Hamamatsu) with Z sections spaced by 0.2 μm.

Cells were segmented based on an in-focus brightfield image using YeaZ (Dietler *et al*, 2020). Falsely segmented cells (e.g. background, or cells falsely combined into one) were manually excluded in Fiji. Only cells in the center of the image, where fluorescence illumination was homogeneous, were included. Flatfielding was not performed. The brightfield images were systematically shifted relative to the fluorescence images and we corrected for that error. Quantification of signals was performed on an average projection of the 23 most in-focus Z-slices (covering 4.6 μm, which is slightly larger than the width of a typical *S. pombe* cell). For each image, the median extracellular background in the same central area of the image was subtracted.

Single-molecule mRNA FISH

For quantification of mRNA by single-molecule fluorescent in-situ hybridization, cultures of asynchronously dividing cells were grown to a concentration of about 1 x 10^7 cells/mL in EMM. Typically, 2 x 10^8 cells were fixed with 4% paraformaldehyde for 30 minutes before being washed three times with ice-cold Buffer B (1.2 M sorbitol, 100 mM potassium phosphate buffer pH 7.5) and stored at 4°C before digestion of the cell wall. Cells were resuspended in spheroblast buffer (1.2 M sorbitol, 0.1 M potassium phosphate, 20 mM vanadyl ribonuclease complex [NEB S1402S], 20 μM beta-mercaptoethanol) and digested with 0.002% 100T zymolyase (US Biological Z1005) for approximately 45–75 minutes. Zymolyase reaction was quenched when addition of water to the cells resulted in around 50% lysed cells. Reactions were quenched with 3 washes of Buffer B. Cell pellets were resuspended in 1 mL of 0.01% Triton X-100 in 1x PBS for 20 minutes and washed three times with Buffer B. For hybridization of probes, approximately 20–25 ng of CAL Fluor red 610 probes targeting ymEGFP or *mad2*, or Quasar 570 probes targeting *mad1* were mixed with

2 μL each of yeast tRNA (Life Technologies) and Salmon sperm DNA (Life Technologies) per reaction. For two-color FISH experiments, 20–25 ng of each probe were combined, resulting in ~50 ng of total FISH probes per reaction. Sequences of probes are given in Table S4. Buffer F (20 **%** formamide, 10 mM sodium phosphate buffer pH 7.2; 45 μL per reaction) was mixed with the probe solution, heated at 95ºC for 3 minutes and allowed to cool to room temperature before mixing with Buffer H (4x saline-sodium citrate (SSC) buffer, 4 mg/mL acetylated BSA, 20 mM vanadyl ribonuclease complex; 50 μL per reaction). Each sample of digested cells was divided into two reactions, each of which was resuspended in 100 μL of this hybridization solution. Resuspended cells were incubated at 37ºC overnight. Cells were washed with 10 % formamide/2x SSC followed by 0.1 % Triton X-100/2x SSC). For DAPI staining, cells were incubated in 1x PBS with 1 μg/mL DAPI for 10 minutes and washed once more with 1x PBS. Cell pellets were mixed with SlowFade Diamond Antifade Mountant (Thermo Scientific, S36972) and mounted on DEPC-cleaned slides using #1.5 glass coverslips. Imaging was performed on a Zeiss AxioImager M1 equipped with Xcite Fire LED illumination (Excelitas), a Zeiss α Plan FLUAR 100x/1.45 oil objective and an ORCA-Flash4.0LT sCMOS camera (Hamamatsu). Images were acquired for 6 μm in Z separated by 0.2 μm steps for each channel. Images of labelled RNA were captured with either an mCherry filter or a 'gold FISH' filter (Chroma, 49304). Additional data on the cell and nucleus were captured with GFP, DAPI and CFP. Images were dark noise-subtracted and flatfield corrected. A custom FIJI macro, using trainable WEKA segmentation (Arganda-Carreras *et al*, 2017), was used to create two-dimensional outlines of cells by CFP autofluorescence and of corresponding nuclei by DAPI. For analyses with cytoplasmic or nuclear RNA counts (except the mad1/mad2 colocalization experiment; Fig 1F), nuclei were re-segmented in three dimensions using a FIJI macro adapted from https://github.com/haesleinhuepf/cca_benchmarking (Robert Haase, MPI-CBG, Dresden). Analysis was limited to cells whose nuclei were entirely contained within the image stack. RNA spot analysis was performed in FISHquant (Mueller *et al*, 2013). Spots were initially detected based on an automatic intensity threshold and filtered with an additional manual threshold following the suggestions of the FISHquant documentation. A subset of cells in each image was cross-checked

manually for successful RNA spot detection.

To measure co-localization of *mad1* and *mad2* mRNA, a two-color FISH experiment was performed targeting *mad1* with gene-specific probes and *mad2*$^{+}$*-ymEGFP* with ymEGFP probes. The three-dimensional coordinates of each spot were recorded and corrected for relative chromatic aberration in Z. Distances were then calculated from each mRNA to its nearest neighbor of the other species within the same cell. In order to determine a distance cut-off for classifying RNA molecules as either co-localized or unpaired, the same two probe sets were used in another two-color FISH experiment in which both probes targeted *mad1*$^{+}$*-ymEGFP*. Nearest-neighbor distances were calculated in the same way, and the distribution of these distances was used to determine the co-localization distance cut-off value. This cut-off was applied to the distances in the original experiment to classify each *mad1* or *mad2* mRNA molecule as co-localized or unpaired.

To test if *mad1* mRNA forms dimers, we used RNA FISH experiments to measure spot intensities and counts of RNA in the cytoplasm in strains with the following genotypes: (1) untagged *mad1*$^{+}$ expressed from the endogenous locus, (2) untagged *mad1*$^{+}$ expressed from the endogenous locus and *mad1*$^{+}$*-ymEGFP* expressed from the exogenous *leu1*$^{+}$ locus, (3) endogenous *mad1*$^{+}$ deleted and *mad1*$^{+}$*-ymEGFP* expressed from the exogenous *leu1*$^{+}$ locus, and (4) *mad1*$^{+}$*-ymEGFP* and *mad3*$^{+}$*-ymEGFP* expressed from the endogenous loci. All samples were hybridized with a combination of *mad1*- and *ymEGFP*-targeting probes in two-color FISH experiments. FISH probe spots were quantified separately for each imaging channel. Colocalized spots of different colors were then paired using the same colocalization method as described for mad1/mad2 colocalization above. Intensity analysis used two measurements of spot intensity provided by FISHquant: the amplitude of the point spread function fit to each spot and the intensity of each spot after background filtering (Mueller *et al.*, 2013). All images quantified from the experiment for each probe set, regardless of genotype, gave consistent distributions of spot intensities, except for one image: while the distributions of spot intensities were qualitatively the same and the counts of spots were consistent with the other images, both its *mad1* and GFP probe spot intensities were shifted substantially lower compared to the other images (including another

image from the same slide and another slide prepared from the same FISH sample). Thus, we decided to remove it from the analysis.

Single-cell RNA counts from FISH experiments were fit with generalized linear mixed models. All models used a Poisson error distribution and natural log link function. The models included the fixed effect cell length and up to three nested random effects (when present): biological replicate (strain), experimental replicate, and microscopy image. Random effects included both random slopes and intercepts for all three variables. Since the relationship between mean RNA count and cell length was approximately linear, cell length was natural log transformed. The transformed cell length was then centered so that a cell of average length had a value of zero.

To test for differences in mean RNA levels between genotypes, the categorical fixed effect variable genotype was added to the model. The interaction between cell length and genotype was also included if a likelihood ratio test comparing models with and without the interaction term showed that it improved the model's ability to explain the data significantly ($p < 0.05$). P-values for the likelihood ratio test were obtained both by comparing the test statistic to a chi-square distribution and generating a null distribution by bootstrapping (1000 replicates) using the 'PBmodcomp' function from the package pbkrtest. In all cases, the results were consistent between the two methods. Only a few models required the interaction term: comparison of wild-type with codon-optimized *mad2* (whole cell, cytoplasmic and nuclear RNA counts), comparison of wild-type with codon-optimized *mad2* + *ste13Δ* (cytoplasmic RNA only) and comparison of untagged and GFP-tagged *mad1*.

Genotype coefficients and corresponding 95 % confidence intervals presented in the paper were exponentiated (e^) and represent the ratio of expected RNA levels between the two genotypes in each comparison. RNA levels were considered significantly different between genotypes if the exponentiated confidence interval excluded 1.

Assay for spindle assembly checkpoint function using *nda3-KM311*

Strains expressing the tubulin mutant *nda3-KM311* were grown in EMM (plus supplements

required for auxotrophic mutations) at 30ºC to a concentration of 0.5–1.0 x 10^7 cells/mL. Cells were diluted with EMM to a final concentration of 7.5 x 10^5 or 1.5 x 10^6 cells/mL. 300 μL of each strain were loaded into a lectin-coated Ibidi μ-Slide glass-bottom chamber and incubated about one hour at 16ºC on the microscope stage prior to imaging. Cells were imaged at 16ºC on a DeltaVision Elite system with a PCO edge sCMOS camera (PCO) and an Olympus 60x/1.42 Plan APO oil objective and EMBL environmental chamber. Images were acquired every 5 minutes for GFP and mCherry over an 18-hour period using an 'optical axis integration' (sum projection) over a 3.2 μm Z-distance.

Plo1-mCherry localizes to spindle pole bodies during mitosis and was used to identify cells in mitosis. Kinetochores cluster with spindle pole bodies in *S. pombe* interphase (Funabiki *et al*, 1993) and dot-like GFP signals were therefore measured in the direct vicinity to Plo1-mCherry. An area of the same size for each cell was used to capture the kinetochore signal and was also used to measure the intensity in the nucleoplasm for background subtraction. GFP intensities from multiple cells were aligned to the time point of Plo1-mCherry appearance and averaged for each timepoint.

Assay for spindle assembly checkpoint function using alp7Δ

Cells were grown in EMM at 25ºC to a concentration of 0.5–1.0 x 10^7 cells/mL, diluted to 1.5 x 10^6 cells/mL, and 300 μL of this dilution were loaded into a lectin-coated ibidi μ-Slide glass-bottom chamber. Cells were incubated on the microscope stage at 30ºC for 35 minutes before imaging. Images were acquired at 30ºC every 55 seconds to 1.5 minutes for 2–3.5 hours using an 'optical axis integration' (sum projection) over a 3.6 μm Z-distance. Cells were segmented based on the brightfield image using YeaZ (Dietler *et al*., 2020). All pixels within the cell were quantified and the 0.1st percentile value was subtracted from the 99.9th percentile value to obtain the "maximal intensity". The localization of Plo1-tdTomato to spindle-pole bodies or Mad1-GFP to kinetochores (Fig S4F) is reflected in higher maximal intensities. Time in mitosis was determined from a custom Matlab script that detects strong increases and decreases in signal. Some cells could not be analyzed in an automated fashion (e.g. due to overlapping other cells) and were analyzed manually. The analysis mode is reported in the source data.

720 **RNA Preparation**

721 Asynchronous *S. pombe* cultures were grown to a final concentration of approximately 0.7–1.5
722 x 10^7 cells/mL at 30ºC in either EMM with 0.2 g/L leucine or YEA. 1 x 10^8 cells were collected by
723 centrifugation, washed once with deionized water, and immediately flash-frozen in liquid nitrogen
724 and stored at –80ºC before processing. RNA was extracted by resuspending samples in 700 μL of
725 ice-cold TES buffer (10 mM Tris HCL pH 7.5, 10 mM EDTA, 0.5 % SDS) and adding 700 μL of
726 acidic phenol chloroform (Fisher Scientific). Samples were immediately vortexed for 20 seconds
727 and incubated for 1 hour at 65ºC. Following incubation, samples were cooled on ice for 1 min,
728 vortexed for an additional 20 seconds and centrifuged for 15 minutes at 16,000 rcf at 4ºC. The RNA
729 was further purified by twice mixing the aqueous supernatant with 700 μL of acidic phenol
730 chloroform and centrifuging the solution in a 5Prime Phase Lock Gel Heavy 2 ml tube (Andwin
731 Scientific) at 16,000 rcf to separate the phases. Following overnight ethanol precipitation, samples
732 were centrifuged at 16,000 rcf for 10 minutes at 4ºC and washed with one equivalent of 70 %
733 ethanol before additional centrifugation. Samples were left to air dry at room temperature and
734 resuspended in nuclease free water before quantification. 50 μg of total RNA was subjected to
735 Dnase treatment (Roche, 10 776 785 001) followed by ethanol precipitation.

736 **Quantitative PCR (qPCR)**

737 For quantitative PCR (qPCR), 1 μg of Dnase-treated total RNA was subjected to Superscript IV
738 cDNA synthesis using oligo $d(T)_{20}$ primers. Transcript abundance was quantified on a QuantStudio
739 6 Real Time PCR system using SYBR® Green PCR Master Mix (ThermoFisher) and gene-specific
740 primers (Supplementary Table S5). To estimate relative expression, raw Ct values (2–3 technical
741 replicates per sample) were averaged and normalized according to the following formula
742 (Hellemans *et al*, 2007; Pfaffl, 2001):

743 $$Relative\ Expression = \frac{\left(efficiency_{target} + 1\right)^{\left(Ct_{target\ control} - Ct_{target\ sample}\right)}}{\left(\prod\left(efficiency_{reference} + 1\right)^{\left(Ct_{reference\ control} - Ct_{reference\ sample}\right)}\right)^{\frac{1}{n}}}$$

744

where "target" is the mRNA of interest, "reference" is the reference gene, "sample" is the sample of interest and "control" is the control sample being normalized to. The denominator is the geometric mean of the reference genes (*act1* and *cdc2*), and efficiencies were estimated from the slopes of four-step, serial 1:5 dilution standard curves.

Determination of mRNA half-life

The mRNA half-life measurement protocol was adapted from Duffy et al. 2015 (Duffy *et al*, 2015) and Chan et al. 2018 (Chan *et al*, 2018). Asynchronous *S. pombe* cultures were grown to a final density of approximately 0.7–0.9 x 10^7 cells/mL at 30ºC in EMM with 0.45 mM uracil and 1.5 mM leucine before collection. 4TU in DMSO (Chem-Impex International) was added at 5 mM final concentration (Eser *et al.*, 2016). Cells (5 x 10^7 cells per sample) were collected by centrifugation, and immediately flash-frozen in liquid nitrogen and stored at –80ºC before processing. Samples were collected from the culture before addition of 4TU (time = 0) and at a series of time points after. For use as a spike-in control, *S. cerevisiae* cultures were grown to a final density of 1.4–3.7 x 10^7 cells/mL in YPD at 30ºC, and then flash-frozen and stored at –80ºC.

RNA extraction was performed as above except flash-frozen samples were initially resuspended in 600 µL of ice-cold TES buffer and 100 µL of resuspended *S. cerevisiae* cells (approximately 5 x 10^7 cells) were added as a spike-in control. Care was taken to add the same amount of *S. cerevisiae* cells to all sample of a time series. After extraction, 200 µg of total RNA was subjected to DNase treatment. Following DNase treatment, 70 µg of RNA was biotinylated with MTSEA biotin-XX (Biotium) as previously described (Chan *et al.*, 2018; Duffy *et al.*, 2015). 50 µg of biotinylated RNA was subjected to oligo d(T) selection using oligo $d(T)_{25}$ magnetic beads (NEB S1419S), substituting SDS and NaCl for the recommended LiDS and LiCl. For streptavidin selection of biotinylated RNA, 500 ng of the oligo d(T) selected mRNA was used. 25 µL of MyOne Streptavidin C1 Dynabeads (ThermoFisher 65001) were washed with 75 µL of 0.1 M NaOH two times, followed by a single 0.1 M NaCl wash, and two additional washes with Buffer 3 (10 mM Tris HCl pH 7.4, 10 mM EDTA, 1 M NaCl). Streptavidin beads were blocked by resuspension in 50 µL of Buffer 3 and 5 µL of 50x

771 Denhardt's reagent. Beads were incubated for 20 minutes with gentle agitation. Following blocking,
772 beads were washed with 75 μL of Buffer 3 four times and resuspended in 75 μL of Buffer 3 with
773 4 μL of 5 M NaCl. 500 ng of mRNA was added to the beads and gently agitated for 15 minutes.
774 Following incubation, beads were washed with 75 μL of Buffer 3 prewarmed to 65ºC, once with
775 Buffer 4 (10 mM Tris-HCl pH 7.4, 1 mM EDTA, 1 % SDS) and twice with 10 % Buffer 3. All flow
776 through was pooled before addition of 20 μg of linear acrylamide (ThermoFisher) followed by
777 ethanol precipitation.

778 Expression relative to the time = 0 sample was quantified using qPCR as described above
779 except 50 ng of recovered unlabeled mRNA was used in the SSIV cDNA synthesis reaction and a
780 single reference gene (*S. cerevisiae ACT1* from the spiked in *S. cerevisiae* cells) was used to
781 normalize expression.

782 To estimate mRNA half-lives (*HL*), several different exponential decay models (adapted from
783 (Chan *et al.*, 2018)) were initially fit to each time series using nonlinear least squares regression:

784 $$fit\ 1 = 2^{-t/HL}$$

785 $$fit\ 2 = efficiency * 2^{-t/HL} + (1 - efficiency)$$

786 $$fit\ 3 = mRNA_0 * 2^{-t/HL}$$

787 *Fit 1* is a simple one-phase exponential decay model. *Fit 2* incorporates an efficiency parameter
788 to accommodate that mRNA levels may not decay to zero (Chan *et al.*, 2018). Finally, to
789 accommodate the effects of non-instantaneous labelling by 4TU on the decay curve, the *fit 3* model
790 was fit without the time = 0 measurements and instead allowed the mRNA level at time = 0 to be
791 estimated as a separate free parameter ($mRNA_0$). Qualitatively, *fit 3* consistently fit the time series
792 best, but all models yielded similar results. To test for statistically significant differences in mRNA
793 half-lives between *ste13+* and *ste13Δ* genotypes, the *fit 3* model was linearized, resulting in the
794 equation

795 $$\ln(mRNA_t) = \ln(mRNA_0) + \frac{-\ln(2)}{HL} t$$

796 and was fit to the combined *ste13+* and *ste13Δ* time series data for each gene (excluding time

= 0) using a general linear mixed model. In the model, natural log transformed relative mRNA expression was modeled as a function of the continuous fixed effects variable time (minutes since 4tU addition), the categorical fixed effect genotype (*ste13*$^{+}$ versus *ste13*Δ), the interaction of time and genotype, and the random effect experimental replicate. The random effect included both random slopes and intercepts to allow the decay rate to vary across experimental replicates.

In the model, half-life is related to the change in expression with respect to time by the formula $HL = -\ln(2)\,/slope$, where slope is the time coefficient for the genotype coded 0 and the sum of the time and interaction coefficients for the genotype coded 1. To simplify the extraction of half-life estimates, models were fit with the genotype coded both ways: first *ste13*$^{+}$ = 0 and then *ste13*Δ = 0. Half-life estimates for *ste13*$^{+}$ and *ste13*Δ genotypes were derived from the version of the model in which the genotype of interest was coded zero using the formula $-\ln(2)\,/[time\ coefficient]$. Corresponding 95 % confidence intervals for the half-life estimates were obtained by using the same formula to rescale the limits of the time coefficient's 95 % bootstrap confidence interval.

Significance testing was done using the 95 % bootstrap confidence interval for the interaction coefficient. A confidence interval that excluded zero indicated significantly different slopes, and thus a difference in half-life between the *ste13*$^{+}$ and *ste13*Δ genotypes.

Codon usage bias calculations

The "Codon occurrence to mRNA Stability Correlation coefficient" (CSC) for each codon was determined as in Presnyak et al. (Presnyak *et al.*, 2015) by calculating a Pearson correlation coefficient between the frequency of occurrence of individual codons in mRNAs and the half-lives of these mRNAs. Coding sequences for *S. pombe* (protein-coding genes, excluding dubious and transposons) were downloaded from Pombase (ASM294v2.62, Release date 2017-01-30) (Lock *et al*, 2019). From this list we excluded "Genome location: mitochondrial", "Genome location: mating_type_region" and "sequence error in genomic data" (PBO:0000129). Five genes lacking start or stop codons were additionally excluded, resulting in a final list of 5,016 genes. We used mRNA half-life data from either Hasan et al. (Hasan *et al.*, 2014) or Eser et al. (Eser *et al.*, 2016),

which are the most recent and comprehensive datasets for *S. pombe*. Out of the 5,016 genes in our list, 4,615 were measured in at least one study and 3,900 in both. Both studies used metabolic labelling and the half-lives correlate with each other (Pearson correlation coefficient 0.50; Spearman's rank correlation 0.81).

A previous study (Harigaya & Parker, 2016) had used the Spearman correlation coefficient to determine CSC values for *S. pombe*, because of outliers in the half-life data. We instead removed outliers from the half-life data, and then used the Pearson correlation coefficient. A comparison between the different strategies is shown in Fig S4C,D. Our criteria for removing outliers were: (i) a value that was more than 10 interquartile ranges above the upper quartile (which removed three genes, based on their value in the Eser et al. data) and (ii) a deviation in rank position of > 2,500 between the two datasets (which removed 13 genes). After the removal of outliers, the Pearson correlation coefficient between the two mRNA half-life datasets was 0.80, the Spearman's rank correlation 0.82. Using either the Hasan et al. or the Eser et al. half-life data for CSC calculation yielded highly similar results (Fig S4C,D). When not otherwise indicated, CSC values obtained from Eser et al. (the more recent study) were used. The CSC_g value for each gene was determined as the arithmetic mean of all codons, excluding the stop codon.

The percentage of optimal codons based on the "classical translational efficiency" (cTE) used the optimality table for *S. pombe* from Pechmann and Frydman (Pechmann & Frydman, 2013). For tAI (tRNA adaptation index), we used the values determined by Tuller et al. (Tuller *et al*, 2010) and also reported in Pechmann and Frydman (Pechmann & Frydman, 2013). The tAI_g value for each gene was determined as the geometric mean of all codons, excluding the stop codon.

CSC values for budding yeast were taken from Carneiro et al. (Carneiro *et al.*, 2019) and only values derived from mRNA half-life measurements within the last 10 years were included (Becskei, Coller, Cramer, Gresham, Struhl, Weis). CSC values for human cells were taken from Wu et al. (Wu *et al.*, 2019). Mad1 and Mad2 sequences from opisthokonts were taken from Vleugel et al. (Vleugel *et al*, 2012). The human Mad1 sequence was swapped for the canonical isoform (UniProt, Q9Y6D9, MD1L1_HUMAN), the *S. pombe* Mad1 sequence was shortened N-terminally by 13

amino acids to start with what is now considered the correct start codon (pombase.org). All sequences shorter than 600 amino acids were omitted for Mad1. Protein sequences were aligned using MAFFT (G-INS-I, using DASH and Mafft-homologs [100 homologs, E=1e-30]) (Katoh *et al*, 2019). Sequences from all species other than *S.c.*, *S.p.* and *H.s.* were deleted for the display of conservation shown in Fig S8. The moving average of CSC values across 9 codons was plotted along the length of the aligned sequence. The null distribution of the moving average was obtained by randomizing the codon order 10,000 times. Observed values that deviated by more than 2 standard deviations from the null mean were marked with filled circles.

Gene expression model – simulations and theoretical predictions

Protein noise predictions (Fig 2C; S2B,C) were made by assuming a constitutively active promoter, and only considering stochastic mRNA and protein synthesis and degradation and ignoring cell growth and division. The coefficient of variation (CV = standard deviation / mean) for protein is calculated as:

$$CV_P = \sqrt{\frac{1}{P} + \frac{1}{M}\frac{kdegP}{(kdegP + kdegM)}}$$

where P is the protein number per cell, M the mRNA number per cell, kdegM the mRNA degradation rate and kdegP the protein degradation rate (Swain, 2004). For the predictions in S2C, we assumed a protein number of 6,000 per cell, mRNA numbers of 1 to 1,000, and we varied RNA degradation rate in a range corresponding to half-lives of 1 to 60 minutes, and protein degradation rate in a range corresponding to half-lives of 15 to 600 minutes, which we consider a physiologically plausible range. Predictions were excluded when mRNA synthesis or protein synthesis rates became unrealistically high. We assumed this to be the case when mRNA synthesis rate was higher than 25 $minute^{-1}$ or protein synthesis rate higher than 20 $mRNA^{-1}$ $minute^{-1}$. Assuming a gene with characteristics similar to a SAC gene (protein number = 6,000, mRNA number = 3.5, protein half-life = 360 minutes, mRNA half-life = 4 minutes) yields a CV prediction of 0.0575. In the figure, we labelled CV predictions less than 0.06 in light grey (low noise) and those equal or higher than 0.06

in dark grey (high noise).

The stochastic simulation of mRNA and protein numbers (Fig 2B) used the same simple underlying model and the Gillespie algorithm in a Matlab script written by Daniel Charlebois and available on MathWorks ("Gillespie's Direct Method Stochastic Simulation Algorithm").

Statistical tests

Data processing performed in R used the packages tidyverse (Wickham *et al*, 2019), alphashape3d, boxcoxmix, broom, broom.mixed, DescTools, geometry, Irescale, mclust, nabor, plyr, readxl, rgl, sf, shotGroups and spatstat. Statistical tests were performed in Prism (GraphPad), or in R using the packages lme4 (Bates *et al*, 2015), MASS, pbkrtest and stats. Figure plots were generated in Prism (GraphPad) or in R using the packages Cairo, cowplot, egg, ggplot2, gridExtra, plotly and lemon.

General linear mixed models and generalized linear mixed models were fit using the functions 'lmer' and 'glmer,' respectively, from the lme4 package. Default function settings were used except for the optimizer in 'glmer,' which was set to 'bobyqa.' Bootstrapping using the function 'bootMer' (10,000 replicates; lme4 package) was used to obtain 95 % confidence intervals for fixed effects model coefficients and 95 % confidence bands for predicted regression curves. Nonlinear least squares regression models, Wilcoxon rank sum tests and t-tests were performed using 'nls', 'wilcox.test' and 't.test,' respectively, from the package stats. Poisson distributions were fit to data frequency distributions using 'fitdistr' from the package MASS.

Sample sizes were not pre-determined. Blinding was not performed, since most analyses were run in an automated fashion.

Data availability

This study includes no data deposited in external repositories.

Material and data created as part of this study are available from the corresponding author without restrictions.

Acknowledgments

We thank Tatiana Boluarte, Hunter Haynie, Jessica Malc, Haoyun Yang, Woong Sik Shin, Wendi Williams, Kenrick Cameron, and Varun Gopala Krishna for their experimental help, Tony Carr's lab for the yEGFP-containing plasmid, Yoshinori Watanabe's lab for yeast strains, Daniel Zenklusen for the FISH protocol, Nick Buchler for sharing an *S. cerevisiae* strain, Young Ho Yun, David Edwards, and Philgeun Jin from the Statistical Applications and Innovations Group (SAIG) at Virginia Tech for advice, as well as Andrea Ciliberto and all members of the Hauf Lab for comments on the manuscript. This work was supported by the National Science Foundation under grant no. 1616247, by the NIH/National Institute of General Medical Sciences under award R35GM119723, and by the Virginia Tech College of Science Dean's Discovery Fund.

Author contributions

Conceptualization: EE, DW, SH; Formal analysis: EE, DW, JR, CM, SH; Funding acquisition: SH; Investigation: EE, DW, JR, CM, EKB, JC, SH; Methodology: EKB, JC; Supervision: SH; Visualization: EE, DW, JR, SH; Writing – Original Draft Preparation: EE, DW, JR, SH; Writing – Review & Editing: EKB, JC.

Conflict of Interest

None.

References

Alfieri C, Chang L, Zhang Z, Yang J, Maslen S, Skehel M, Barford D (2016) Molecular basis of APC/C regulation by the spindle assembly checkpoint. *Nature* 536: 431-436

Aravind L, Koonin EV (1998) The HORMA domain: a common structural denominator in mitotic checkpoints, chromosome synapsis and DNA repair. *Trends Biochem Sci* 23: 284-286

Arganda-Carreras I, Kaynig V, Rueden C, Eliceiri KW, Schindelin J, Cardona A, Sebastian Seung H (2017) Trainable Weka Segmentation: a machine learning tool for microscopy pixel classification. *Bioinformatics* 33: 2424-2426

Bähler J, Wu JQ, Longtine MS, Shah NG, McKenzie A, 3rd, Steever AB, Wach A, Philippsen P, Pringle JR (1998) Heterologous modules for efficient and versatile PCR-based gene targeting in Schizosaccharomyces pombe. *Yeast* 14: 943-951

Baker DJ, Chen J, van Deursen JM (2005) The mitotic checkpoint in cancer and aging: what have mice taught us? *Curr Opin Cell Biol* 17: 583-589

Bates D, Machler M, Bolker BM, Walker SC (2015) Fitting Linear Mixed-Effects Models Using lme4. *J Stat Softw* 67: 1-48

Baybay EK, Esposito E, Hauf S (2020) Pomegranate: 2D segmentation and 3D reconstruction for fission yeast and other radially symmetric cells. *Sci Rep* 10: 16580

Bertolini M, Fenzl K, Kats I, Wruck F, Tippmann F, Schmitt J, Auburger JJ, Tans S, Bukau B, Kramer G (2021) Interactions between nascent proteins translated by adjacent ribosomes drive homomer assembly. *Science* 371: 57-64

Buschauer R, Matsuo Y, Sugiyama T, Chen YH, Alhusaini N, Sweet T, Ikeuchi K, Cheng J, Matsuki Y, Nobuta R *et al* (2020) The Ccr4-Not complex monitors the translating ribosome for codon optimality. *Science* 368

Carneiro RL, Requião RD, Rossetto S, Domitrovic T, Palhano FL (2019) Codon stabilization coefficient as a metric to gain insights into mRNA stability and codon bias and their relationships with translation. *Nucleic Acids Research* 47: 2216-2228

Chan LY, Mugler CF, Heinrich S, Vallotton P, Weis K (2018) Non-invasive measurement of mRNA decay reveals translation initiation as the major determinant of mRNA stability. *Elife* 7

Chao WC, Kulkarni K, Zhang Z, Kong EH, Barford D (2012) Structure of the mitotic checkpoint complex. *Nature* 484: 208-213

Chen RH, Brady DM, Smith D, Murray AW, Hardwick KG (1999) The spindle checkpoint of budding yeast depends on a tight complex between the Mad1 and Mad2 proteins. *Mol Biol Cell* 10: 2607-2618

950 Cheng J, Maier KC, Avsec Ž, Rus P, Gagneur J (2017) Cis-regulatory elements explain most of the
951 mRNA stability variation across genes in yeast. *Rna* 23: 1648-1659

952 Christiano R, Nagaraj N, Fröhlich F, Walther TC (2014) Global proteome turnover analyses of the
953 Yeasts S. cerevisiae and S. pombe. *Cell Rep* 9: 1959-1965

954 Chung E, Chen RH (2002) Spindle checkpoint requires Mad1-bound and Mad1-free Mad2. *Mol Biol*
955 *Cell* 13: 1501-1511

956 Cohen-Sharir Y, McFarland JM, Abdusamad M, Marquis C, Bernhard SV, Kazachkova M, Tang H,
957 Ippolito MR, Laue K, Zerbib J *et al* (2021) Aneuploidy renders cancer cells vulnerable to mitotic
958 checkpoint inhibition. *Nature*

959 Dietler N, Minder M, Gligorovski V, Economou AM, Joly D, Sadeghi A, Chan CHM, Koziński M,
960 Weigert M, Bitbol AF *et al* (2020) A convolutional neural network segments yeast microscopy
961 images with high accuracy. *Nat Commun* 11: 5723

962 Dobles M, Liberal V, Scott ML, Benezra R, Sorger PK (2000) Chromosome missegregation and
963 apoptosis in mice lacking the mitotic checkpoint protein Mad2. *Cell* 101: 635-645

964 Duffy EE, Rutenberg-Schoenberg M, Stark CD, Kitchen RR, Gerstein MB, Simon MD (2015)
965 Tracking Distinct RNA Populations Using Efficient and Reversible Covalent Chemistry. *Mol Cell* 59:
966 858-866

967 Duncan CD, Mata J (2011) Widespread cotranslational formation of protein complexes. *PLoS*
968 *Genet* 7: e1002398

969 Eser P, Wachutka L, Maier KC, Demel C, Boroni M, Iyer S, Cramer P, Gagneur J (2016)
970 Determinants of RNA metabolism in the Schizosaccharomyces pombe genome. *Mol Syst Biol* 12:
971 857

972 Faesen AC, Thanasoula M, Maffini S, Breit C, Müller F, van Gerwen S, Bange T, Musacchio A
973 (2017) Basis of catalytic assembly of the mitotic checkpoint complex. *Nature* 542: 498-502

974 Fischer J, Song YS, Yosef N, di Iulio J, Churchman LS, Choder M (2020) The yeast
975 exoribonuclease Xrn1 and associated factors modulate RNA polymerase II processivity in 5' and 3'
976 gene regions. *J Biol Chem* 295: 11435-11454

977 Funabiki H, Hagan I, Uzawa S, Yanagida M (1993) Cell cycle-dependent specific positioning and
978 clustering of centromeres and telomeres in fission yeast. *J Cell Biol* 121: 961-976

979 Funk LC, Zasadil LM, Weaver BA (2016) Living in CIN: Mitotic Infidelity and Its Consequences for
980 Tumor Promotion and Suppression. *Dev Cell* 39: 638-652

981 Garcia-Martinez J, Medina DA, Bellvis P, Sun M, Cramer P, Chavez S, Perez-Ortin JE (2021) The
982 total mRNA concentration buffering system in yeast is global rather than gene-specific. *RNA* 27:
983 1281-1290

984 Gordon DJ, Resio B, Pellman D (2012) Causes and consequences of aneuploidy in cancer. *Nat*
985 *Rev Genet* 13: 189-203

986 Gross F, Bonaiuti P, Hauf S, Ciliberto A (2018) Implications of alternative routes to APC/C inhibition
987 by the mitotic checkpoint complex. *PLoS Comput Biol* 14: e1006449

988 Haimovich G, Medina DA, Causse SZ, Garber M, Millan-Zambrano G, Barkai O, Chavez S, Perez-
989 Ortin JE, Darzacq X, Choder M (2013) Gene expression is circular: factors for mRNA degradation
990 also foster mRNA synthesis. *Cell* 153: 1000-1011

991 Hanson G, Coller J (2018) Codon optimality, bias and usage in translation and mRNA decay. *Nat*
992 *Rev Mol Cell Biol* 19: 20-30

993 Harigaya Y, Parker R (2016) Analysis of the association between codon optimality and mRNA
994 stability in Schizosaccharomyces pombe. *BMC Genomics* 17: 895

995 Hasan A, Cotobal C, Duncan CD, Mata J (2014) Systematic analysis of the role of RNA-binding
996 proteins in the regulation of RNA stability. *PLoS Genet* 10: e1004684

997 Hausser J, Mayo A, Keren L, Alon U (2019) Central dogma rates and the trade-off between
998 precision and economy in gene expression. *Nat Commun* 10: 68

999 He F, Celik A, Wu C, Jacobson A (2018) General decapping activators target different subsets of
1000 inefficiently translated mRNAs. *Elife* 7

1001 Heinrich S, Geissen EM, Kamenz J, Trautmann S, Widmer C, Drewe P, Knop M, Radde N,
1002 Hasenauer J, Hauf S (2013) Determinants of robustness in spindle assembly checkpoint signalling.
1003 *Nat Cell Biol* 15: 1328-1339

1004 Heinrich S, Sewart K, Windecker H, Langegger M, Schmidt N, Hustedt N, Hauf S (2014) Mad1
1005 contribution to spindle assembly checkpoint signalling goes beyond presenting Mad2 at
1006 kinetochores. *EMBO Rep* 15: 291-298

1007 Hellemans J, Mortier G, De Paepe A, Speleman F, Vandesompele J (2007) qBase relative
1008 quantification framework and software for management and automated analysis of real-time
1009 quantitative PCR data. *Genome Biol* 8: R19

1010 Holland AJ, Cleveland DW (2009) Boveri revisited: chromosomal instability, aneuploidy and
1011 tumorigenesis. *Nat Rev Mol Cell Biol* 10: 478-487

1012 Horikoshi Y, Habu T, Matsumoto T (2013) An E2 enzyme Ubc11 is required for ubiquitination of
1013 Slp1/Cdc20 and spindle checkpoint silencing in fission yeast. *Cell Cycle* 12: 961-971

1014 Jacobs JZ, Ciccaglione KM, Tournier V, Zaratiegui M (2014) Implementation of the CRISPR-Cas9
1015 system in fission yeast. *Nat Commun* 5: 5344

1016 Ji W, Luo Y, Ahmad E, Liu ST (2018) Direct interactions of mitotic arrest deficient 1 (MAD1) domains
1017 with each other and MAD2 conformers are required for mitotic checkpoint signaling. *J Biol Chem*
1018 293: 484-496

1019 Jin DY, Spencer F, Jeang KT (1998) Human T cell leukemia virus type 1 oncoprotein Tax targets
1020 the human mitotic checkpoint protein MAD1. *Cell* 93: 81-91

1021 Jungfleisch J, Nedialkova DD, Dotu I, Sloan KE, Martinez-Bosch N, Bruning L, Raineri E, Navarro
1022 P, Bohnsack MT, Leidel SA *et al* (2017) A novel translational control mechanism involving RNA
1023 structures within coding sequences. *Genome Res* 27: 95-106

1024 Katoh K, Rozewicki J, Yamada KD (2019) MAFFT online service: multiple sequence alignment,
1025 interactive sequence choice and visualization. *Brief Bioinform* 20: 1160-1166

1026 Kim S, Sun H, Tomchick DR, Yu H, Luo X (2012) Structure of human Mad1 C-terminal domain
1027 reveals its involvement in kinetochore targeting. *Proc Natl Acad Sci U S A* 109: 6549-6554

1028 Kops G, Snel B, Tromer EC (2020) Evolutionary Dynamics of the Spindle Assembly Checkpoint in
1029 Eukaryotes. *Curr Biol* 30: R589-r602

1030 Kops GJPL, Foltz DR, Cleveland DW (2004) Lethality to human cancer cells through massive
1031 chromosome loss by inhibition of the mitotic checkpoint. *Proceedings of the National Academy of*
1032 *Sciences of the United States of America* 101: 8699-8704

1033 Kulukian A, Han JS, Cleveland DW (2009) Unattached kinetochores catalyze production of an
1034 anaphase inhibitor that requires a Mad2 template to prime Cdc20 for BubR1 binding. *Dev Cell* 16:
1035 105-117

1036 Lad L, Lichtsteiner S, Hartman JJ, Wood KW, Sakowicz R (2009) Kinetic analysis of Mad2-Cdc20
1037 formation: conformational changes in Mad2 are catalyzed by a C-Mad2-ligand complex.
1038 *Biochemistry* 48: 9503-9515

1039 Lara-Gonzalez P, Westhorpe FG, Taylor SS (2012) The spindle assembly checkpoint. *Curr Biol* 22:
1040 R966-980

1041 Liu Y, Yang Q, Zhao F (2021) Synonymous but not Silent: The Codon Usage Code for Gene
1042 Expression and Protein Folding. *Annu Rev Biochem*

1043 Lock A, Rutherford K, Harris MA, Hayles J, Oliver SG, Bahler J, Wood V (2019) PomBase 2018:
1044 user-driven reimplementation of the fission yeast database provides rapid and intuitive access to
1045 diverse, interconnected information. *Nucleic Acids Res* 47: D821-D827

1046 Luo X, Tang Z, Rizo J, Yu H (2002) The Mad2 spindle checkpoint protein undergoes similar major
1047 conformational changes upon binding to either Mad1 or Cdc20. *Mol Cell* 9: 59-71

1048 Luo X, Tang Z, Xia G, Wassmann K, Matsumoto T, Rizo J, Yu H (2004) The Mad2 spindle
1049 checkpoint protein has two distinct natively folded states. *Nat Struct Mol Biol* 11: 338-345

1050 Mapelli M, Massimiliano L, Santaguida S, Musacchio A (2007) The Mad2 conformational dimer:
1051 structure and implications for the spindle assembly checkpoint. *Cell* 131: 730-743

1052 Michel L, Diaz-Rodriguez E, Narayan G, Hernando E, Murty VVVS, Benezra R (2004) Complete
1053 loss of the tumor suppressor MAD2 causes premature cyclin B degradation and mitotic failure in
1054 human somatic cells. *Proceedings of the National Academy of Sciences of the United States of*
1055 *America* 101: 4459-4464

1056 Mueller F, Senecal A, Tantale K, Marie-Nelly H, Ly N, Collin O, Basyuk E, Bertrand E, Darzacq X,
1057 Zimmer C (2013) FISH-quant: automatic counting of transcripts in 3D FISH images. *Nat Methods*
1058 10: 277-278

1059 Musacchio A (2015) The Molecular Biology of Spindle Assembly Checkpoint Signaling Dynamics.
1060 *Curr Biol* 25: R1002-1018

1061 Narula A, Ellis J, Taliaferro JM, Rissland OS (2019) Coding regions affect mRNA stability in human
1062 cells. *RNA* 25: 1751-1764

1063 Neymotin B, Ettorre V, Gresham D (2016) Multiple Transcript Properties Related to Translation
1064 Affect mRNA Degradation Rates in Saccharomyces cerevisiae. *G3 (Bethesda)* 6: 3475-3483

1065 Padovan-Merhar O, Nair GP, Biaesch AG, Mayer A, Scarfone S, Foley SW, Wu AR, Churchman
1066 LS, Singh A, Raj A (2015) Single mammalian cells compensate for differences in cellular volume
1067 and DNA copy number through independent global transcriptional mechanisms. *Mol Cell* 58: 339-
1068 352

1069 Panasenko OO, Somasekharan SP, Villanyi Z, Zagatti M, Bezrukov F, Rashpa R, Cornut J, Iqbal
1070 J, Longis M, Carl SH *et al* (2019) Co-translational assembly of proteasome subunits in NOT1-
1071 containing assemblysomes. *Nat Struct Mol Biol* 26: 110-120

1072 Pechmann S, Frydman J (2013) Evolutionary conservation of codon optimality reveals hidden
1073 signatures of cotranslational folding. *Nat Struct Mol Biol* 20: 237-243

1074 Petersen J, Russell P (2016) Growth and the Environment of Schizosaccharomyces pombe. *Cold*
1075 *Spring Harb Protoc* 2016: pdb.top079764

1076 Pfaffl MW (2001) A new mathematical model for relative quantification in real-time RT-PCR. *Nucleic*
1077 *Acids Res* 29: e45

1078 Piano V, Alex A, Stege P, Maffini S, Stoppiello GA, Huis In 't Veld PJ, Vetter IR, Musacchio A (2021)
1079 CDC20 assists its catalytic incorporation in the mitotic checkpoint complex. *Science* 371: 67-71

1080 Pines J (2011) Cubism and the cell cycle: the many faces of the APC/C. *Nat Rev Mol Cell Biol* 12:
1081 427-438

1082 Presnyak V, Alhusaini N, Chen YH, Martin S, Morris N, Kline N, Olson S, Weinberg D, Baker KE,
1083 Graveley BR *et al* (2015) Codon optimality is a major determinant of mRNA stability. *Cell* 160: 1111-

1084 1124

1085 Quinton RJ, DiDomizio A, Vittoria MA, Kotynkova K, Ticas CJ, Patel S, Koga Y, Vakhshoorzadeh
1086 J, Hermance N, Kuroda TS *et al* (2021) Whole-genome doubling confers unique genetic
1087 vulnerabilities on tumour cells. *Nature*

1088 R-Core-Team, 2020. R: a language and environment for stastical computing. . R foundation for
1089 stastical Computing Vienna, Austria.

1090 Radhakrishnan A, Chen YH, Martin S, Alhusaini N, Green R, Coller J (2016) The DEAD-Box Protein
1091 Dhh1p Couples mRNA Decay and Translation by Monitoring Codon Optimality. *Cell* 167: 122-
1092 132.e129

1093 Raj A, Peskin CS, Tranchina D, Vargas DY, Tyagi S (2006) Stochastic mRNA synthesis in
1094 mammalian cells. *PLoS Biol* 4: e309

1095 Rodriguez-Bravo V, Maciejowski J, Corona J, Buch HK, Collin P, Kanemaki MT, Shah JV, Jallepalli
1096 PV (2014) Nuclear pores protect genome integrity by assembling a premitotic and Mad1-dependent
1097 anaphase inhibitor. *Cell* 156: 1017-1031

1098 Roguev A, Wiren M, Weissman JS, Krogan NJ (2007) High-throughput genetic interaction mapping
1099 in the fission yeast Schizosaccharomyces pombe. *Nat Methods* 4: 861-866

1100 Rubio A, Ghosh S, Mülleder M, Ralser M, Mata J (2020) Ribosome profiling reveals ribosome
1101 stalling on tryptophan codons and ribosome queuing upon oxidative stress in fission yeast. *Nucleic*
1102 *Acids Research*

1103 Ryan SD, Britigan EM, Zasadil LM, Witte K, Audhya A, Roopra A, Weaver BA (2012) Up-regulation
1104 of the mitotic checkpoint component Mad1 causes chromosomal instability and resistance to
1105 microtubule poisons. *Proc Natl Acad Sci U S A* 109: E2205-2214

1106 Saint M, Bertaux F, Tang W, Sun XM, Game L, Köferle A, Bähler J, Shahrezaei V, Marguerat S
1107 (2019) Single-cell imaging and RNA sequencing reveal patterns of gene expression heterogeneity
1108 during fission yeast growth and adaptation. *Nat Microbiol* 4: 480-491

1109 Sato M, Koonrugsa N, Toda T, Vardy L, Tournier S, Millar JB (2003) Deletion of Mia1/Alp7 activates
1110 Mad2-dependent spindle assembly checkpoint in fission yeast. *Nat Cell Biol* 5: 764-766; author
1111 reply 766

1112 Sauna ZE, Kimchi-Sarfaty C (2011) Understanding the contribution of synonymous mutations to
1113 human disease. *Nat Rev Genet* 12: 683-691

1114 Schukken KM, Zhu Y, Bakker PL, Koster MH, Harkema L, Youssef SA, de Bruin A, Foijer F (2021)
1115 Acute systemic loss of Mad2 leads to intestinal atrophy in adult mice. *Sci Rep* 11: 68

1116 Schuyler SC, Wu YF, Kuan VJ (2012) The Mad1-Mad2 balancing act--a damaged spindle
1117 checkpoint in chromosome instability and cancer. *J Cell Sci* 125: 4197-4206

1118 Schvartzman JM, Sotillo R, Benezra R (2010) Mitotic chromosomal instability and cancer: mouse
1119 modelling of the human disease. *Nat Rev Cancer* 10: 102-115

1120 Schwarz A, Beck M (2019) The Benefits of Cotranslational Assembly: A Structural Perspective.
1121 *Trends Cell Biol* 29: 791-803

1122 Schweizer N, Ferrás C, Kern DM, Logarinho E, Cheeseman IM, Maiato H (2013) Spindle assembly
1123 checkpoint robustness requires Tpr-mediated regulation of Mad1/Mad2 proteostasis. *J Cell Biol*
1124 203: 883-893

1125 Sczaniecka M, Feoktistova A, May KM, Chen JS, Blyth J, Gould KL, Hardwick KG (2008) The
1126 spindle checkpoint functions of Mad3 and Mad2 depend on a Mad3 KEN box-mediated interaction
1127 with Cdc20-anaphase-promoting complex (APC/C). *J Biol Chem* 283: 23039-23047

1128 Shiber A, Döring K, Friedrich U, Klann K, Merker D, Zedan M, Tippmann F, Kramer G, Bukau B
1129 (2018) Cotranslational assembly of protein complexes in eukaryotes revealed by ribosome profiling.
1130 *Nature* 561: 268-272

1131 Simonetta M, Manzoni R, Mosca R, Mapelli M, Massimiliano L, Vink M, Novak B, Musacchio A,
1132 Ciliberto A (2009) The influence of catalysis on mad2 activation dynamics. *PLoS Biol* 7: e10

1133 Sironi L, Mapelli M, Knapp S, De Antoni A, Jeang KT, Musacchio A (2002) Crystal structure of the
1134 tetrameric Mad1-Mad2 core complex: implications of a 'safety belt' binding mechanism for the
1135 spindle checkpoint. *Embo j* 21: 2496-2506

1136 Sironi L, Melixetian M, Faretta M, Prosperini E, Helin K, Musacchio A (2001) Mad2 binding to Mad1
1137 and Cdc20, rather than oligomerization, is required for the spindle checkpoint. *Embo j* 20: 6371-
1138 6382

1139 Sudakin V, Chan GK, Yen TJ (2001) Checkpoint inhibition of the APC/C in HeLa cells is mediated
1140 by a complex of BUBR1, BUB3, CDC20, and MAD2. *J Cell Biol* 154: 925-936

1141 Suijkerbuijk SJ, van Osch MH, Bos FL, Hanks S, Rahman N, Kops GJ (2010) Molecular causes for
1142 BUBR1 dysfunction in the human cancer predisposition syndrome mosaic variegated aneuploidy.
1143 *Cancer Res* 70: 4891-4900

1144 Sun M, Schwalb B, Pirkl N, Maier KC, Schenk A, Failmezger H, Tresch A, Cramer P (2013) Global
1145 analysis of eukaryotic mRNA degradation reveals Xrn1-dependent buffering of transcript levels.
1146 *Mol Cell* 52: 52-62

1147 Sun XM, Bowman A, Priestman M, Bertaux F, Martinez-Segura A, Tang W, Whilding C, Dormann
1148 D, Shahrezaei V, Marguerat S (2020) Size-Dependent Increase in RNA Polymerase II Initiation
1149 Rates Mediates Gene Expression Scaling with Cell Size. *Curr Biol* 30: 1217-1230.e1217

1150 Supek F, Miñana B, Valcárcel J, Gabaldón T, Lehner B (2014) Synonymous mutations frequently
1151 act as driver mutations in human cancers. *Cell* 156: 1324-1335

1152 Swain PS (2004) Efficient attenuation of stochasticity in gene expression through post-
1153 transcriptional control. *J Mol Biol* 344: 965-976

1154 Thattai M, van Oudenaarden A (2001) Intrinsic noise in gene regulatory networks. *Proc Natl Acad*
1155 *Sci U S A* 98: 8614-8619

1156 Timmers HTM, Tora L (2018) Transcript Buffering: A Balancing Act between mRNA Synthesis and
1157 mRNA Degradation. *Mol Cell* 72: 10-17

1158 Tuller T, Waldman YY, Kupiec M, Ruppin E (2010) Translation efficiency is determined by both
1159 codon bias and folding energy. *Proceedings of the National Academy of Sciences* 107: 3645-3650

1160 Varetti G, Guida C, Santaguida S, Chiroli E, Musacchio A (2011) Homeostatic control of mitotic
1161 arrest. *Mol Cell* 44: 710-720

1162 Vink M, Simonetta M, Transidico P, Ferrari K, Mapelli M, De Antoni A, Massimiliano L, Ciliberto A,
1163 Faretta M, Salmon ED *et al* (2006) In vitro FRAP identifies the minimal requirements for Mad2
1164 kinetochore dynamics. *Curr Biol* 16: 755-766

1165 Vleugel M, Hoogendoorn E, Snel B, Kops GJ (2012) Evolution and function of the mitotic
1166 checkpoint. *Dev Cell* 23: 239-250

1167 Watson AT, Garcia V, Bone N, Carr AM, Armstrong J (2008) Gene tagging and gene replacement
1168 using recombinase-mediated cassette exchange in Schizosaccharomyces pombe. *Gene* 407: 63-
1169 74

1170 Weber R, Chung MY, Keskeny C, Zinnall U, Landthaler M, Valkov E, Izaurralde E, Igreja C (2020)
1171 4EHP and GIGYF1/2 Mediate Translation-Coupled Messenger RNA Decay. *Cell Rep* 33: 108262

1172 Webster MW, Chen YH, Stowell JAW, Alhusaini N, Sweet T, Graveley BR, Coller J, Passmore LA
1173 (2018) mRNA Deadenylation Is Coupled to Translation Rates by the Differential Activities of Ccr4-
1174 Not Nucleases. *Mol Cell* 70: 1089-1100 e1088

1175 Wickham H (2016) *ggplot2: Elegant Graphics for Data Analysis*. Springer-Verlag New York

1176 Wickham H, Averick M, Bryan J, Chang W, McGowan L, François R, Grolemund G, Hayes A, Henry
1177 L, Hester J *et al* (2019) Welcome to the Tidyverse.

1178 Wu Q, Medina SG, Kushawah G, DeVore ML, Castellano LA, Hand JM, Wright M, Bazzini AA
1179 (2019) Translation affects mRNA stability in a codon-dependent manner in human cells. *Elife* 8

1180 Zacharias DA, Violin JD, Newton AC, Tsien RY (2002) Partitioning of lipid-modified monomeric
1181 GFPs into membrane microdomains of live cells. *Science* 296: 913-916

1182 Zenklusen D, Larson DR, Singer RH (2008) Single-RNA counting reveals alternative modes of
1183 gene expression in yeast. *Nat Struct Mol Biol* 15: 1263-1271

1184 Zhurinsky J, Leonhard K, Watt S, Marguerat S, Bähler J, Nurse P (2010) A coordinated global
1185 control over cellular transcription. *Curr Biol* 20: 2010-2015

1186

Figure legends

Figure 1. Low steady-state mRNA numbers of checkpoint genes *mad1*, *mad2* and *mad3*.

(A) Overview of the interactions between Mad1, Mad2 and Mad3. **(B)** Schematic of marker-less GFP-tagging at the endogenous locus and representative live cell images of Mad1-, Mad2-, and Mad3-GFP strains (average intensity projections). **(C)** Representative images of single molecule mRNA FISH (smFISH) staining of *S. pombe* using probes against GFP (red). DNA was stained with DAPI (blue). The gamma-value was adjusted to make the cytoplasm visible; cell shapes are outlined in blue. **(D)** Frequency distribution of mRNA numbers per cell determined by smFISH; combined data from 3, 4, and 5 experiments, respectively, shown separately in Fig EV1C; n = number of cells. Curves show fit to a Poisson distribution. **(E)** Frequency distribution of mRNA numbers per cell using FISH probes against the endogenous genes and using either strains expressing the GFP-tagged gene or the endogenous, untagged gene. The difference for *mad1* is statistically significant, that for *mad2* is not (Fig EV1E). A lower mRNA number for untagged *mad1* was also observed in a different strain. **(F)** Co-staining by smFISH using probes against *mad1* and GFP either in a strain expressing *mad1*-GFP as a positive control or in a strain expressing wild-type *mad1* and *mad2*-GFP. Cytoplasmic *mad1* (green) or GFP mRNA spots (magenta) were quantified as co-localizing or not with the respective other. For the *mad1*-GFP strain, 544 cells and a total of 1,641 *mad1* spots and 1,839 GFP spots were analyzed; 48 cells were not considered since they did not contain at least one spot of each type in the cytoplasm. For the *mad1 mad2*-GFP strain, 571 cells and a total of 1,107 mad1 spots and 1,537 GFP spots were analyzed; 158 cells were not considered since they did not contain at least one spot of each type in the cytoplasm.

Figure 2. The checkpoint genes *mad1*, *mad2* and *mad3* combine short mRNA and long protein half-lives, explaining low noise.

(A) Cellular protein noise (coefficient of variation, CV = std / mean) in live-cell microscopy images

of *S. pombe*; n = 7 images (Nmt1-GFP), 11 (Mad1-GFP), 19 (Mad2-GFP), 10 (Mad3-GFP); single images had 16 – 79 GFP-positive and 6 – 94 GFP-negative (control) cells. Mad1, Mad2, and Mad3 all showed significantly lower noise than Nmt1 (Wilcoxon rank sum test; all $p < 0.001$). **(B)** Simulations of stochastic gene expression noise from selected mRNA/protein half-life combinations assuming a constantly active promoter (see Methods). Synthesis rates were set to obtain a mean mRNA number of 4 per cell, and a mean protein number of 6000 per cell. The x-axis of each graph shows time, the y-axis shows mRNA number per cell (blue) or protein number per cell (black). **(C)** Theoretical prediction for the coefficient of variation (CV = std / mean) of the protein number per cell, assuming different mRNA and protein half-lives, using the same underlying model as in B. Synthesis rates were adjusted to maintain a mean mRNA number per cell of 3.5, and a mean protein number per cell of 6000 (approx. 100 nM). **(D)** mRNA abundances by qPCR following metabolic labeling and removal of the labeled pool (two independent experiments). Lines are regression curves from generalized linear mixed model fits, excluding the measurements at t = 0 in order to accommodate for non-instantaneous labeling by 4tU. *Act1* and *ecm33* were used as long and short half-life controls, respectively; qPCR was performed for the endogenous mRNAs. Half-lives (95 % confidence interval): *mad1* 5.6 min (4.3 - 8.4), *mad2* 7.7 min (6.2 - 10.4), *mad3* 5.2 min (4.3 - 6.9), *act1* 61.8 min (37.2 - 172.3), *ecm33* 5.0 min (4.5 - 5.7). **(E)** Protein abundances after translation shut-off with cycloheximide (CHX); n = 3 experiments, error bars = std. Lines indicate fit to a one-phase exponential decay. Cdc2 and Cdc13 were used as long and short half-life controls, respectively. Immunoblots for the endogenous proteins (no tag). A representative experiment shown in Fig S2E.

Figure 3. Codon optimization increases the steady-state mRNA numbers of *mad2* and *mad3*.

(A) The mean CSC value for each *S. pombe* gene (CSC_g) relative to protein number per cell by mass spectrometry (Carpy et al., 2014). CSC was determined using the mRNA half-life data by Eser et al. (Eser et al., 2016) as described in Methods. Colored dots highlight proteins of interest. For Mad2 and Bub1, no protein abundance data was available. **(B)** Cumulative frequency

distribution of the CSC_g values for protein-coding *S. pombe* genes. The position of spindle assembly checkpoint genes is highlighted. **(C)** Schematic of the *mad2* and *mad3* genes. Regions coding for important structural features are highlighted. Black lines in the bottom graph indicate synonymous codon changes in the codon-optimized version. **(D)** Scatter plots of whole cell RNA counts versus cell length. Solid lines are regression curves from generalized linear mixed model fits (gray: wild type, black: codon-optimized or *ste13Δ*). Dashed lines: 95 % bootstrap confidence bands for the regression curves. Model estimates of the ratio relative to wild-type mRNA are included with bootstrap 95 % confidence interval in brackets. Two to five replicates per genotype. **(E)** Time course of RNA abundances by qPCR following metabolic labeling and removal of the labeled pool (two independent experiments). Solid lines: regression curves from generalized linear mixed model fits (dark = *ste13+*, light = *ste13Δ*), excluding t = 0 to accommodate for non-instantaneous labeling by 4tU. Shaded area: 95 % bootstrap confidence band for *ste13+*; dashed lines: 95 % bootstrap confidence band for *ste13Δ*. Half-life estimates are included with 95 % bootstrap confidence intervals in brackets. See Fig EV2C for additional statistics. The *ste13+* data are the same as in Fig 2.

Figure 4. Codon optimization increases the protein concentrations of Mad2 and Mad3.

(A) Immunoblot of *S. pombe* protein extracts from cells expressing wild-type (WT) or codon-optimized (co) Mad2-GFP or Mad3-GFP probed with antibodies against GFP and Cdc2 (loading control). Lanes 3–5 are a 1:1 dilution series of the extract from cells expressing the codon-optimized version. **(B)** Immunoblot of protein extracts from wild-type (WT) or *ste13Δ* strains probed with antibodies against Mad2, Mad3 and tubulin (loading control). A 1:1 dilution series was loaded for quantification. **(C)** Estimates of the protein concentration relative to wild-type conditions from experiments such as in (A) and (B). Bars are experimental replicates, dots are technical replicates. Two-sided t-tests: p = 0.03 (Mad2-co), 0.004 (Mad3-co), 0.82 (Mad2 *ste13Δ*), 0.15 (Mad3 *ste13Δ*). **(D)** Whole-cell GFP concentration from individual live cell fluorescence microscopy experiments (a.u. = arbitrary units). Boxes show median and interquartile range (IQR). Codon-optimized

concentration significantly higher than wild type for both genes (GLMM). Mad2-GFP: n = 468 and 413; Mad2-co-GFP: n = 206 and 366; Mad3-GFP: n = 224 and 127; Mad3-co-GFP: n = 160, 450 and 212 cells. **(E)** Representative images from one of the experiments in (D). A single Z-slice is shown; cells are outlined in grey.

Figure 5. Codon optimization and *ste13* deletion do not significantly affect the steady-state mRNA number of mad1.

(A) Schematic of the *mad1* gene. Regions coding for important structural features are highlighted. Black lines in the bottom graph indicate synonymous codon changes in the codon-optimized version. **(B)** Scatter plots of whole cell mRNA counts versus cell length. Solid lines are regression curves from generalized linear mixed model fits (gray: wild type, black: codon-optimized or *ste13Δ*). Dashed lines: 95 % bootstrap confidence bands for the regression curves. Model estimates of the ratio relative to wild-type mRNA are included with bootstrap 95 % confidence interval in brackets. Two to three replicates per genotype. **(C)** Time course of RNA abundances by qPCR following metabolic labeling and removal of the labeled pool (two independent experiments). Solid lines: regression curves from generalized linear mixed model fits (dark = *ste13⁺*, light = *ste13Δ*), excluding t = 0 to accommodate for non-instantaneous labeling by 4tU. Shaded area: 95 % bootstrap confidence band for *ste13⁺*; dashed lines: 95 % bootstrap confidence band for *ste13Δ*. Half-life estimates are included with 95 % bootstrap confidence intervals in brackets. See Fig EV4E for additional statistics. The *ste13⁺* data are the same as in Fig 2. **(D)** Comparison between mean CSC values for selected genes (CSC_g) and mRNA half-life measured with or without deletion of *ste13*. mRNA half-life estimates from Figs 3E, 5C and EV4D.

Figure 6. Codon identity in mad1 is important for proper protein concentration.

(A) Immunoblot of *S. pombe* protein extracts from cells expressing wild-type (WT) or codon-optimized (co) Mad1-GFP probed with antibodies against GFP and Cdc2 (loading control). Lanes 3–5 are a dilution series of the extract from wild-type cells. **(B)** Immunoblot of protein extracts from

wild-type (WT) or *ste13Δ* strains probed with antibodies against Mad1 and tubulin (loading control). A 1:1 dilution series was loaded for quantification. Tubulin blot is the same as in Fig 4B. **(C)** Estimates of the protein concentration relative to wild-type conditions from experiments such as in (A) and (B). Bars are experimental replicates, dots are technical replicates. Blue lines indicate the mean of all experiments. Two-sided t-tests: p = 0.005 (Mad1-co, n = 4 experimental replicates); p = 0.16 (Mad1 *ste13Δ*, n = 2). **(D)** Whole-cell GFP concentration from individual live cell fluorescence microscopy experiments (a.u. = arbitrary units). Boxplots show median and interquartile range (IQR); lines extend to values no further than 1.5 times the IQR from the first and third quartile, respectively. Codon-optimized concentration significantly lower than wild type (generalized linear mixed model). Mad1-GFP: n = 197 and 224; Mad1-co-GFP: n = 80 and 377 cells. **(E)** Representative images from one of the experiments in (D). An average projection of three Z-slices is shown; cells are outlined in grey. **(F)** Live-cell imaging for time spent in mitosis. The *alp7⁺* gene was deleted to increase the likelihood of spindle assembly checkpoint activation. Localization of Plo1-tdTomato to spindle pole bodies was used to judge entry into and exit from mitosis (also see Figure S4). Exp1: n = 73 (WT) and 94 cells (co); Exp2: n = 126 (WT) and 152 cells (co). Difference between WT and co: p = 0.14 (Exp1) and 0.15 (Exp2) by Kolmogorov-Smirnov test.

Figure 7. Mad1 homodimers assemble co-translationally.

(A) Top: Immunoprecipitation (IP) with anti-GFP or anti-Mad1 from extracts of haploid *S. pombe* cells expressing both untagged and GFP-tagged Mad1, probed with antibodies against Mad1 and tubulin; in = input (2.5 % of extract for IP), sup = supernatant after IP. Bottom: Comparison between the observed (obs.) and the expected (expect.) ratio between Mad1-GFP and untagged Mad1 in the IP given their ratio in the input (see Fig EV6A); 2 and 1 experiments respectively. One more GFP-IP from the same strain was unquantifiable, because no second band was visible in the IP. **(B)** Schematic illustrating that Mad1-Mad1 complex assembly likely takes place co-translationally with only proteins synthesized from the same mRNA being combined. **(C)** Top: Anti-GFP immunoprecipitation (IP) and Strep pull-down (PD) from extracts of diploid cells expressing Mad1-

GFP and Mad1-Strep from the two endogenous loci; membrane probed with anti-Mad1; in = input (7 % of extract for IP/PD), sup = supernatant after IP/PD. Bottom: as in (A), 2 experiments each. See Fig EV6 for a quantified experiment. The experiment shown at the top and two more GFP-IPs from the same strain were unquantifiable, because no second band was visible in the IP. **(D)** In vitro translation (IVT) of Mad1-flag-His and untagged Mad1 in the presence of ^{35}S-labelled Methionine and Cysteine, followed by Mad1 immunoprecipitation (IP) or His pull-down (PD); in = input (9.5 % of extract for IP/PD), sup = supernatant after IP/PD. An IVT with only untagged Mad1 was used to check for specificity of the His PD (right side). Shown is the autoradiograph after SDS-PAGE with quantification of the Mad1-flag-His to untagged Mad1 ratio in select lanes. **(E)** Test for mRNA dimerization by single molecule mRNA FISH; probes against mad1 and GFP. Top: Schematic of genotypes. Example pictures in Fig EV6. Bottom left: Intensity of cytoplasmic *mad1* mRNA spots in the different strains. For the 2 copy strain, a *mad1* spot was classified as *mad1*-GFP if it was colocalizing with a GFP spot, and as *mad1* otherwise. Colors as indicated in the schematic. Vertical solid line: peak of each density plot; dashed line: theoretical position of a double-intensity peak. Number of spots analyzed: *mad1* (1 copy strain) = 921, *mad1* (2 copy strain) = 637, *mad1*-GFP (2 copy strain) = 982, *mad1*-GFP (1 copy strain) = 1699. Bottom right: Counts of cytoplasmic *mad1* or *mad1*-GFP mRNA from the same experiment with generalized linear mixed model fits as lines. Number of cells: 1 copy strain mad1 = 478, 2 copy strain = 327, 1 copy strain mad1-GFP = 466. **(F)** Experiment similar to (E), except that cells expressing both Mad1-GFP and Mad3-GFP from the respective endogenous locus were probed with FISH probes against *mad1* and GFP mRNA. A GFP spot was classified as *mad1*-GFP if it was colocalizing with a *mad1* spot (arrowheads), and as *mad3*-GFP otherwise. The intensity of GFP spots was quantified. Vertical solid line: peak of each density plot; dashed line: theoretical position of a double-intensity peak. Number of spots analyzed: *mad1*-GFP = 987, *mad3*-GFP = 1299 spots.

Figure 1

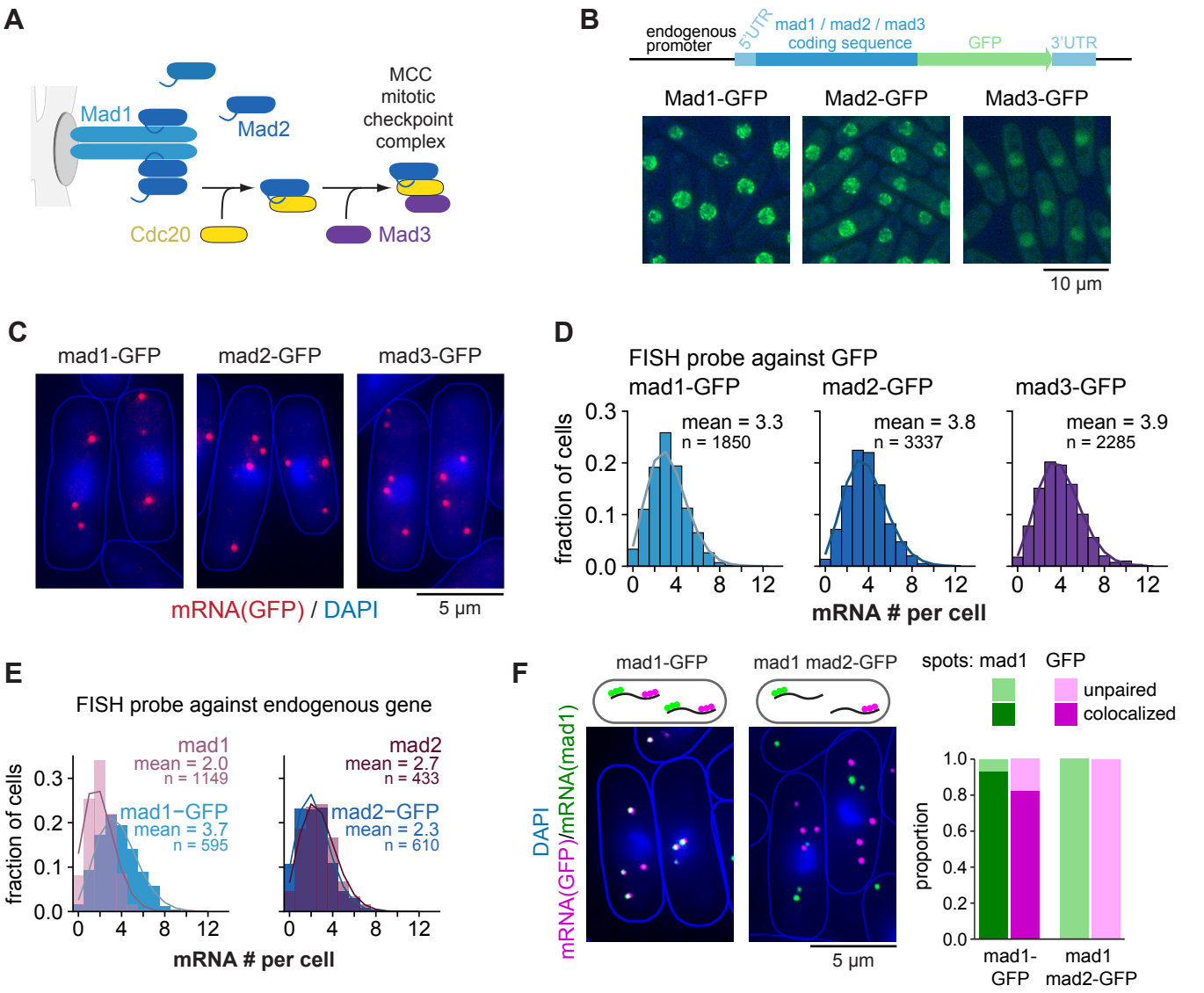

Figure 1. Low steady-state mRNA numbers of checkpoint genes *mad1*, *mad2* and *mad3.*
(A) Overview of the interactions between Mad1, Mad2 and Mad3. **(B)** Schematic of marker-less GFP-tagging at the endogenous locus and representative live cell images of Mad1-, Mad2-, and Mad3-GFP strains (average intensity projections). **(C)** Representative images of single molecule mRNA FISH (smFISH) staining using probes against GFP (red). DNA was stained with DAPI (blue). The gamma-value was adjusted to make the cytoplasm visible; cell shapes are outlined in blue. **(D)** Frequency distribution of mRNA numbers per cell determined by smFISH; combined data from 3, 4, and 5 experiments, respectively, shown separately in Fig EV1C; n = number of cells. Curves show fit to a Poisson distribution. **(E)** Frequency distribution of mRNA numbers per cell using FISH probes against the endogenous genes and using either strains expressing the GFP-tagged gene or the endogenous, untagged gene. The difference for mad1 is statistically significant, that for mad2 is not (Fig EV1E). A lower mRNA number for untagged mad1 was also observed in a different strain. **(F)** Co-staining by smFISH using probes against mad1 and GFP either in a strain expressing *mad1-GFP* as a positive control or in a strain expressing wild-type *mad1* and *mad2-GFP*. Cytoplasmic mad1 (green) or GFP mRNA spots (magenta) were quantified as co-localizing or not with the respective other. For the *mad1-GFP* strain, 544 cells and a total of 1,641 mad1 spots and 1,839 GFP spots were analyzed; 48 cells were not considered since they did not contain at least one spot of each type in the cytoplasm. For the *mad1 mad2-GFP* strain, 571 cells and a total of 1,107 mad1 spots and 1,537 GFP spots were analyzed; 158 cells were not considered since they did not contain at least one spot of each type in the cytoplasm.

Figure 2

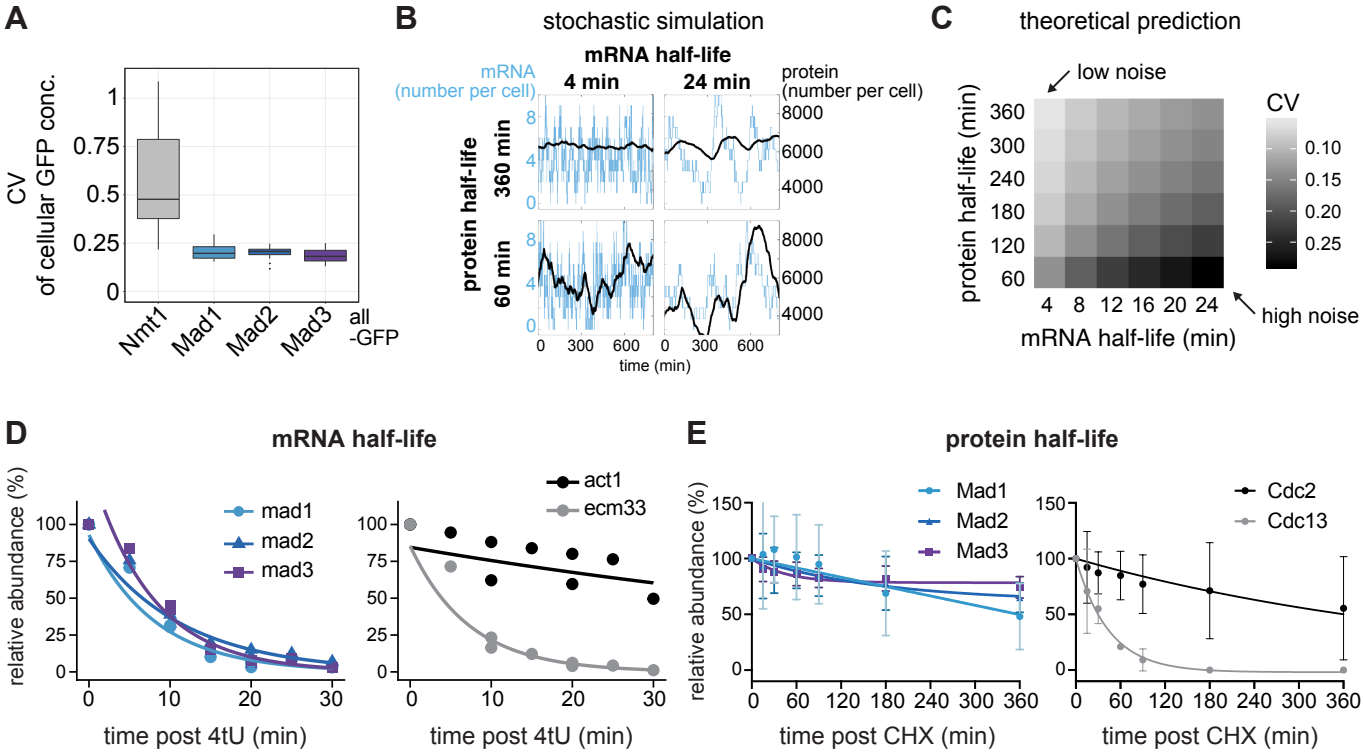

Figure 2. The checkpoint genes *mad1*, *mad2* and *mad3* combine short mRNA and long protein half-lives, explaining low noise.

(A) Cellular protein noise (coefficient of variation, CV = std / mean) in live-cell microscopy images; n = 7 images (Nmt1-GFP), 11 (Mad1-GFP), 19 (Mad2-GFP), 10 (Mad3-GFP); single images had 16 – 79 GFP-positive and 6 – 94 GFP-negative (control) cells. Mad1, Mad2, and Mad3 all showed significantly lower noise than Nmt1 (Wilcoxon rank sum test; all $p < 0.001$).
(B) Simulations of stochastic gene expression noise from selected mRNA/protein half-life combinations assuming a constantly active promoter (see Methods). Synthesis rates were set to obtain a mean mRNA number of 4 per cell, and a mean protein number of 6000 per cell. The x-axis of each graph shows time, the y-axis shows mRNA number per cell (blue) or protein number per cell (black). **(C)** Theoretical prediction for the coefficient of variation (CV = std / mean) of the protein number per cell, assuming different mRNA and protein half-lives, using the same underlying model as in B. Synthesis rates were adjusted to maintain a mean mRNA number per cell of 3.5, and a mean protein number per cell of 6000 (approx. 100 nM). **(D)** mRNA abundances by qPCR following metabolic labeling and removal of the labeled pool (two independent experiments). Lines are regression curves from generalized linear mixed model fits, excluding the measurements at t = 0 in order to accommodate for non-instantaneous labeling by 4tU. *Act1* and *ecm33* were used as long and short half-life controls, respectively; qPCR was performed for the endogenous mRNAs. Half-lives (95 % confidence interval): *mad1* 5.6 min (4.3 - 8.4), *mad2* 7.7 min (6.2 - 10.4), *mad3* 5.2 min (4.3 - 6.9), *act1* 61.8 min (37.2 - 172.3), *ecm33* 5.0 min (4.5 - 5.7). **(E)** Protein abundances after translation shut-off with cycloheximide (CHX); n = 3 experiments, error bars = std. Lines indicate fit to a one-phase exponential decay. Cdc2 and Cdc13 were used as long and short half-life controls, respectively. Immunoblots for the endogenous proteins (no tag). A representative experiment shown in Fig S2E.

Figure 3

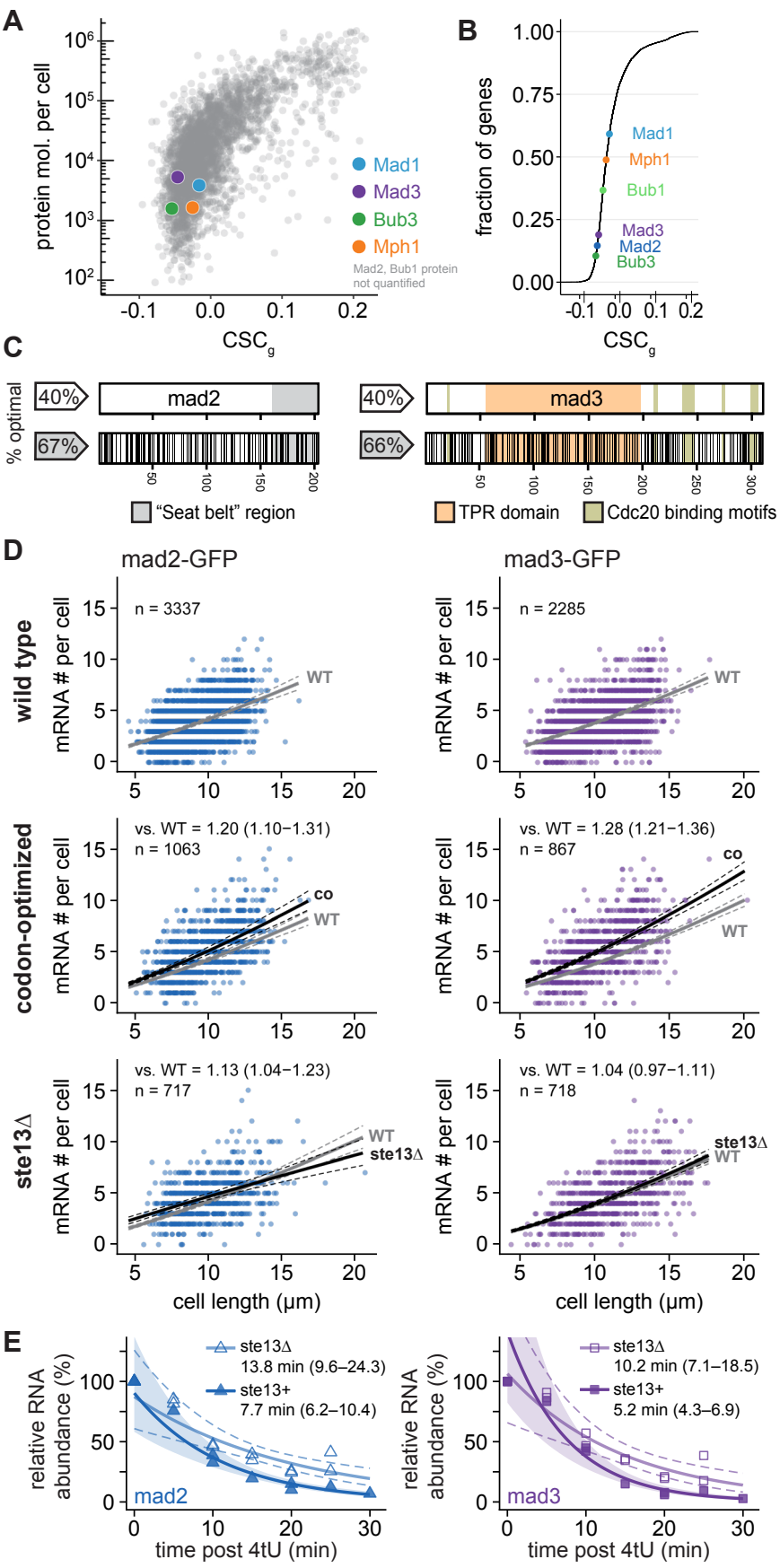

Figure 3. Codon optimization increases the steady-state mRNA numbers of *mad2* and *mad3*.

(A) The mean CSC value for each *S. pombe* gene (CSC$_g$) relative to protein number per cell by mass spectrometry (Carpy *et al.*, 2014). CSC was determined using the mRNA half-life data by Eser *et al.* (Eser *et al.*, 2016) as described in Methods. Colored dots highlight proteins of interest. For Mad2 and Bub1, no protein abundance data was available. **(B)** Cumulative frequency distribution of the CSC$_g$ values for protein-coding *S. pombe* genes. The position of spindle assembly checkpoint genes is highlighted. **(C)** Schematic of the *mad2* and *mad3* genes. Regions coding for important structural features are highlighted. Black lines in the bottom graph indicate synonymous codon changes in the codon-optimized version. **(D)** Scatter plots of whole cell RNA counts versus cell length. Solid lines are regression curves from generalized linear mixed model fits (gray: wild type, black: codon-optimized or *ste13*Δ). Dashed lines: 95 % bootstrap confidence bands for the regression curves. Model estimates of the ratio relative to wild-type mRNA are included with bootstrap 95 % confidence interval in brackets. Two to five replicates per genotype. **(E)** Time course of RNA abundances by qPCR following metabolic labeling and removal of the labeled pool (two independent experiments). Solid lines: regression curves from generalized linear mixed model fits (dark = *ste13*$^+$, light = *ste13*Δ), excluding t = 0 to accommodate for non-instantaneous labeling by 4tU. Shaded area: 95 % bootstrap confidence band for *ste13*$^+$; dashed lines: 95 % bootstrap confidence band for *ste13*Δ. Half-life estimates are included with 95% bootstrap confidence intervals in brackets. See Fig EV2C for additional statistics. The *ste13*$^+$ data are the same as in Fig 2.

Figure 4

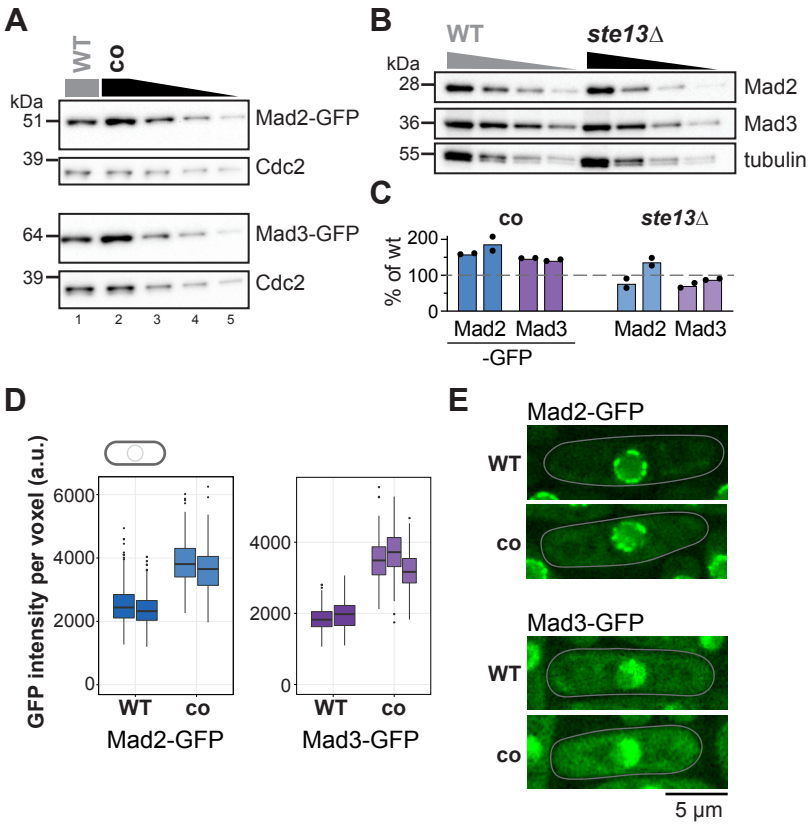

Figure 4. Codon optimization increases the protein concentrations of Mad2 and Mad3. **(A)** Immunoblot of protein extracts from cells expressing wild-type (WT) or codon-optimized (co) Mad2-GFP or Mad3-GFP probed with antibodies against GFP and Cdc2 (loading control). Lanes 3–5 are a 1:1 dilution series of the extract from cells expressing the codon-optimized version. **(B)** Immunoblot of protein extracts from wild-type (WT) or *ste13*Δ strains probed with antibodies against Mad2, Mad3 and tubulin (loading control). A 1:1 dilution series was loaded for quantification. **(C)** Estimates of the protein concentration relative to wild-type conditions from experiments such as in (A) and (B). Bars are experimental replicates, dots are technical replicates. Two-sided t-tests: p = 0.03 (Mad2-co), 0.004 (Mad3-co), 0.82 (Mad2 *ste13*Δ), 0.15 (Mad3 *ste13*Δ). **(D)** Whole-cell GFP concentration from individual live cell fluorescence microscopy experiments (a.u. = arbitrary units). Boxes show median and interquartile range (IQR). Codon-optimized concentration significantly higher than wild type for both genes (GLMM). Mad2-GFP: n = 468 and 413; Mad2-co-GFP: n = 206 and 366; Mad3-GFP: n = 224 and 127; Mad3-co-GFP: n = 160, 450 and 212 cells. **(E)** Representative images from one of the experiments in (D). A single Z-slice is shown; cells are outlined in grey.

Figure 5

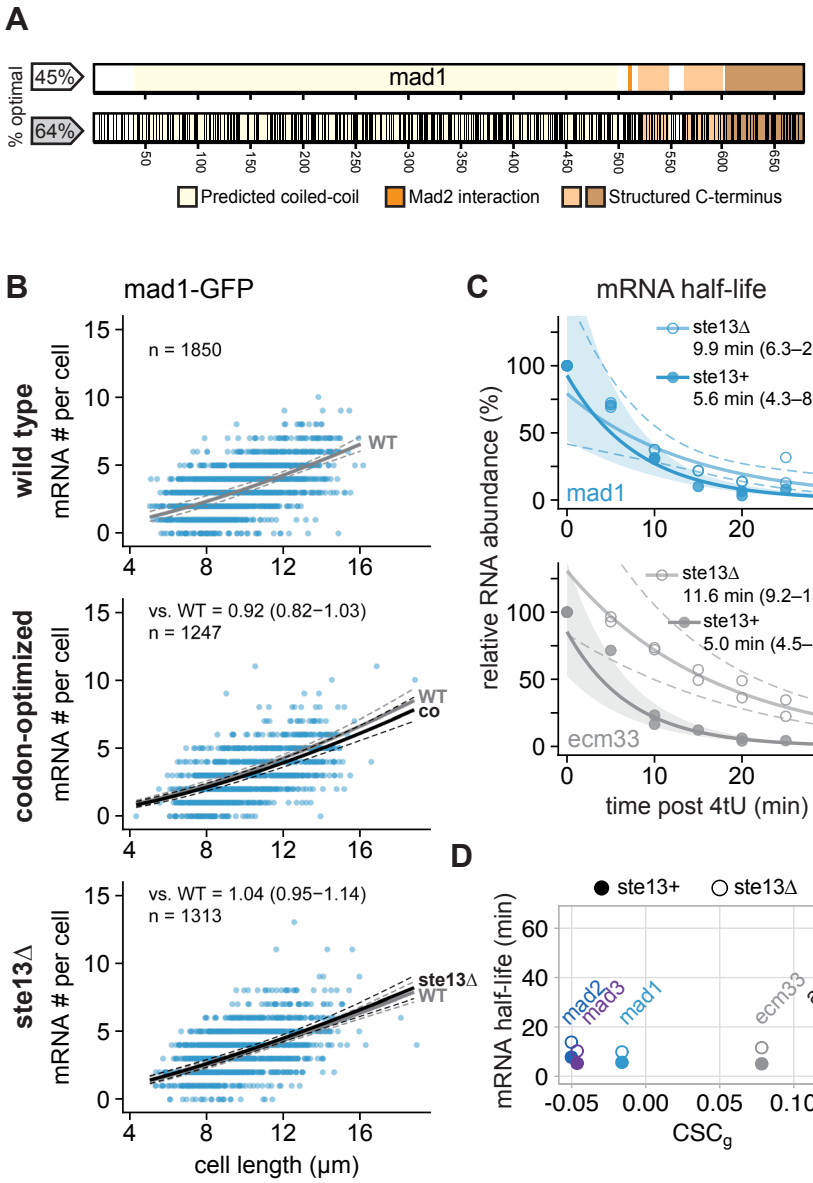

Figure 5. Codon optimization and *ste13* deletion do not significantly affect the steady-state mRNA number of *mad1*.
(A) Schematic of the *mad1* gene. Regions coding for important structural features are highlighted. Black lines in the bottom graph indicate synonymous codon changes in the codon-optimized version. **(B)** Scatter plots of whole cell mRNA counts versus cell length. Solid lines are regression curves from generalized linear mixed model fits (gray: wild type, black: codon-optimized or *ste13*Δ). Dashed lines: 95 % bootstrap confidence bands for the regression curves. Model estimates of the ratio relative to wild-type mRNA are included with bootstrap 95 % confidence interval in brackets. Two to three replicates per genotype. **(C)** Time course of RNA abundances by qPCR following metabolic labeling and removal of the labeled pool (two independent experiments). Solid lines: regression curves from generalized linear mixed model fits (dark = *ste13*$^+$, light = *ste13*Δ), excluding t = 0 to accommodate for non-instantaneous labeling by 4tU. Shaded area: 95 % bootstrap confidence band for *ste13*$^+$; dashed lines: 95 % bootstrap confidence band for *ste13*Δ. Half-life estimates are included with 95 % bootstrap confidence intervals in brackets. See Fig EV4E for additional statistics. The *ste13*$^+$ data are the same as in Fig 2. **(D)** Comparison between mean CSC values for selected genes (CSC_g) and mRNA half-life measured with or without deletion of *ste13*. mRNA half-life estimates from Figs 3E, 5C and EV4D.

Figure 6

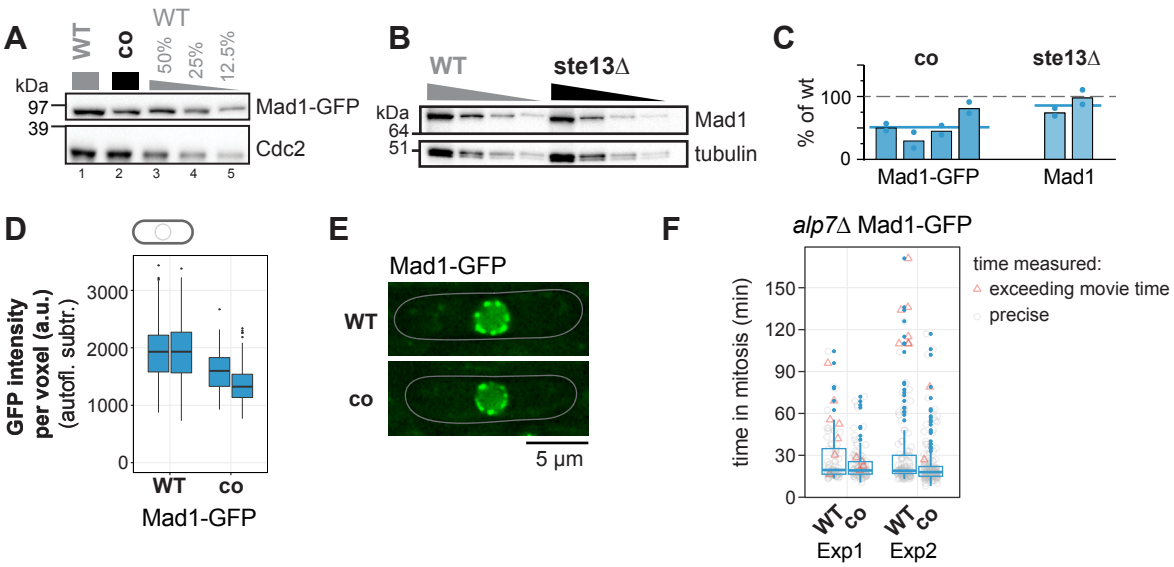

Figure 6. Codon identity in *mad1* is important for proper protein concentration.
(A) Immunoblot of protein extracts from cells expressing wild-type (WT) or codon-optimized (co) Mad1-GFP probed with antibodies against GFP and Cdc2 (loading control). Lanes 3–5 are a dilution series of the extract from wild-type cells. **(B)** Immunoblot of protein extracts from wild-type (WT) or *ste13*Δ strains probed with antibodies against Mad1 and tubulin (loading control). A 1:1 dilution series was loaded for quantification. Tubulin blot is the same as in Fig 4B. **(C)** Estimates of the protein concentration relative to wild-type conditions from experiments such as in (A) and (B). Bars are experimental replicates, dots are technical replicates. Blue lines indicate the mean of all experiments. Two-sided t-tests: p = 0.005 (Mad1-co, n = 4 experimental replicates); p = 0.16 (Mad1 *ste13*Δ, n = 2). **(D)** Whole-cell GFP concentration from individual live cell fluorescence microscopy experiments (a.u. = arbitrary units). Boxplots show median and interquartile range (IQR); lines extend to values no further than 1.5 times the IQR from the first and third quartile, respectively. Codon-optimized concentration significantly lower than wild type (generalized linear mixed model). Mad1-GFP: n = 197 and 224; Mad1-co-GFP: n = 80 and 377 cells. **(E)** Representative images from one of the experiments in (D). An average projection of three Z-slices is shown; cells are outlined in grey. **(F)** Live-cell imaging for time spent in mitosis. The *alp7*$^{+}$ gene was deleted to increase the likelihood of spindle assembly checkpoint activation. Localization of Plo1-tdTomato to spindle pole bodies was used to judge entry into and exit from mitosis (also see Figure S4). Exp1: n = 73 (WT) and 94 cells (co); Exp2: n = 126 (WT) and 152 cells (co). Difference between WT and co: p = 0.14 (Exp1) and 0.15 (Exp2) by Kolmogorov-Smirnov test.

Figure 7

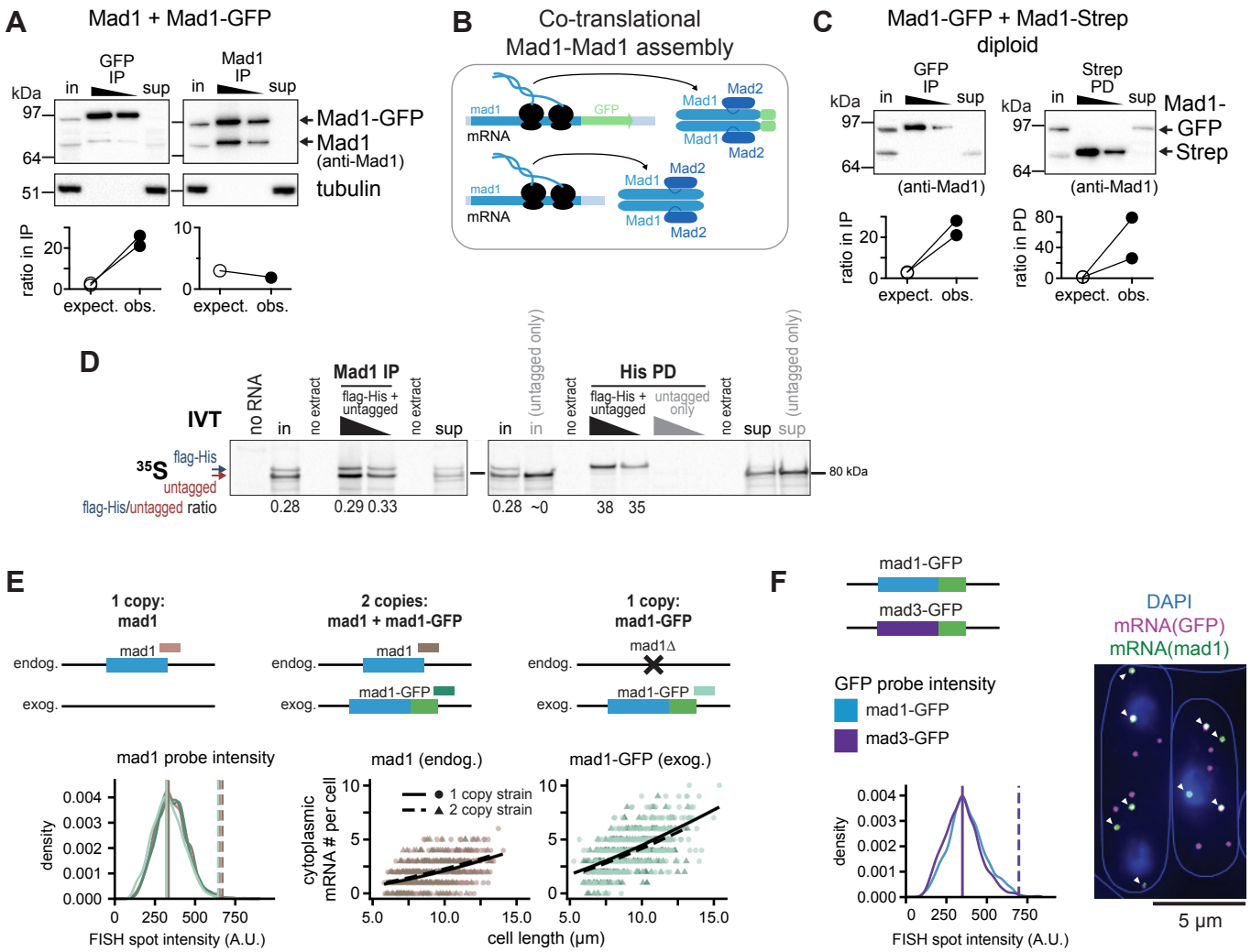

Figure 7. Mad1 homodimers assemble co-translationally.

(A) Top: Immunoprecipitation (IP) with anti-GFP or anti-Mad1 from extracts of haploid cells expressing both untagged and GFP-tagged Mad1, probed with antibodies against Mad1 and tubulin; in = input (2.5 % of extract for IP), sup = supernatant after IP. Bottom: Comparison between the observed (obs.) and the expected (expect.) ratio between Mad1-GFP and untagged Mad1 in the IP given their ratio in the input (see Fig EV6A); 2 and 1 experiments respectively. One more GFP-IP from the same strain was unquantifiable, because no second band was visible in the IP. **(B)** Schematic illustrating that Mad1-Mad1 complex assembly likely takes place co-translationally with only proteins synthesized from the same mRNA being combined. **(C)** Top: Anti-GFP immunoprecipitation (IP) and Strep pull-down (PD) from extracts of diploid cells expressing Mad1-GFP and Mad1-Strep from the two endogenous loci; membrane probed with anti-Mad1; in = input (7 % of extract for IP/PD), sup = supernatant after IP/PD. Bottom: as in (A), 2 experiments each. See Fig EV6 for a quantified experiment. The experiment shown at the top and two more GFP-IPs from the same strain were unquantifiable, because no second band was visible in the IP. **(D)** In vitro translation (IVT) of Mad1-flag-His and untagged Mad1 in the presence of ^{35}S-labelled Methionine and Cysteine, followed by Mad1 immunoprecipitation (IP) or His pull-down (PD); in = input (9.5 % of extract for IP/PD), sup = supernatant after IP/PD. An IVT with only untagged Mad1 was used to check for specificity of the His PD (right side). Shown is the autoradiograph after SDS-PAGE with quantification of the Mad1-flag-His to untagged Mad1 ratio in select lanes. **(E)** Test for mRNA dimerization by single molecule mRNA FISH; probes against mad1 and GFP. Top: Schematic of genotypes. Example pictures in Fig EV6. Bottom left: Intensity of cytoplasmic mad1 mRNA spots in the different strains. For the 2 copy strain, a mad1 spot was classified as mad1-GFP if it was colocalizing with a GFP spot, and as mad1 otherwise. Colors as indicated in the schematic. Vertical solid line: peak of each density plot; dashed line: theoretical position of a double-intensity peak. Number of spots analyzed: mad1 (1 copy strain) = 921, mad1 (2 copy strain) = 637, mad1-GFP (2 copy strain) = 982, mad1-GFP (1 copy strain) = 1699. Bottom right: Counts of cytoplasmic mad1 or mad1-GFP mRNA from the same experiment with generalized linear mixed model fits as lines. Number of cells: 1 copy strain mad1 = 478, 2 copy strain = 327, 1 copy strain mad1-GFP = 466. **(F)** Experiment similar to (E), except that cells expressing both Mad1-GFP and Mad3-GFP from the respective endogenous locus were probed with FISH probes against mad1 and GFP mRNA. A GFP spot was classified as mad1-GFP if it was colocalizing with a mad1 spot (arrowheads), and as mad3-GFP otherwise. The intensity of GFP spots was quantified. Vertical solid line: peak of each density plot; dashed line: theoretical position of a double-intensity peak. Number of spots analyzed: mad1-GFP = 987, mad3-GFP = 1299 spots.